AGU PUBLICATIONS

JGR

Journal of Geophysical Research: Earth Surface

RESEARCH ARTICLE
10.1002/2013JF003068

Key Points:
- An initial phase of shallow mass movements was targeted by a 16 m long core
- A plumite interval was interpreted to have acted as the basal glide plane
- Movement was inferred to have started within contouritic sediments above

Correspondence to:
N. J. Baeten,
Nicole.Baeten@ngu.no

Citation:
Baeten, N. J., J. S. Laberg, M. Vanneste, C. F. Forsberg, T. J. Kvalstad, M. Forwick, T. O. Vorren, and H. Haflidason (2014), Origin of shallow submarine mass movements and their glide planes—Sedimentological and geotechnical analyses from the continental slope off northern Norway, *J. Geophys. Res. Earth Surf.*, *119*, 2335–2360, doi:10.1002/2013JF003068.

Received 20 DEC 2013
Accepted 5 OCT 2014
Accepted article online 8 OCT 2014
Published online 4 NOV 2014

Origin of shallow submarine mass movements and their glide planes—Sedimentological and geotechnical analyses from the continental slope off northern Norway

Nicole J. Baeten[1,2], Jan Sverre Laberg[1], Maarten Vanneste[3], Carl Fredrik Forsberg[3], Tore J. Kvalstad[3], Matthias Forwick[1], Tore O. Vorren[1,4], and Haflidi Haflidason[5]

[1]Department of Geology, University of Tromsø, Tromsø, Norway, [2]Now at Geological Survey of Norway, Trondheim, Norway, [3]Norwegian Geotechnical Institute and International Centre for Geohazards, Oslo, Norway, [4]Deceased 16 June 2013, [5]Department of Earth Science, University of Bergen, Bergen, Norway

Abstract Submarine landslides are often characterized by a basal surface of rupture parallel to the stratigraphy, in which downslope movement is initiated. However, little is known about the sedimentology and physical properties of the sediments within these surfaces. In this study, we present a multiproxy analysis of the sediments collected from a giant piston core penetrating a shallow submarine mass transport deposit, in combination with high-resolution seismoacoustic data to identify and characterize the basal glide plane and the weaker sediments in which movement was initiated. The initial phase of instability consists of a single fracture that formed due to the downslope movement of a mostly intact slab of sediments. The 16 m long core, comprising mostly undisturbed massive and laminated ice-rafted debris-rich clay penetrated this slab. The base of the slab is characterized by a high-amplitude semicontinuous reflection visible on the subbottom profiler data at about 12.5 m depth, interpreted to originate from the glide plane on top of a plumite deposit. This plumite has dilative behavior with pore pressure decrease with increasing shear strain and high undrained shear strength. Movement probably started within contouritic sediments immediately above the glide plane, characterized by higher sensitivities and higher water contents. The occurrence of the mass movements documented in this study are likely affected by the presence of a submarine landslide complex directly downslope. The slide scar of this landslide complex promoted retrogressive movement farther upslope and progressive spreading of strain softening along the slide base and in the slide mass. Numerical models (infinite slope, BING, and retrogressive slope models) illustrate that the present-day continental slope is essentially stable and allow reconstruction of the failure processes when initiated by an external trigger.

1. Introduction

Submarine mass movements are important processes sculpting continental margins. They are responsible for redepositing large volumes of sediments from the upper slopes and the outer shelves into the deep ocean basins. High-resolution geophysical mapping (including swath bathymetry and 2-D/3-D seismics) of continental margins and fjords systematically reveals that mass movement processes are common phenomena worldwide, ranging from giant landslides [e.g., *Embley*, 1980; *O'Leary*, 1996; *Piper et al*., 1999; *Laberg et al*., 2003; *Mosher et al*., 2004; *Solheim et al*., 2005; *Vanneste et al*., 2006; *Krastel et al*., 2012] to smaller-scale instabilities [e.g., *Lastras et al*., 2004; *L'Heureux et al*., 2012, 2013]. The slide scar geomorphology is often complex and indicative of retrogressive development in multiple phases.

Hazard assessment of submarine landslides involves understanding (i) the preconditioning factors with respect to the regional geological history and tectonic framework, (ii) the actual triggers and their frequency of occurrence, (iii) the deformation processes and landslide dynamics, and (iv) the consequences for, e.g., infrastructure and coastal impacts (tsunamis) [e.g., *Hampton et al*., 1996; *Canals et al*., 2004]. Knowledge of preconditions of sediments that fail and the actual triggering mechanisms has improved following extensive studies throughout the last decade including *Canals et al*. [2004], *Bryn et al*. [2005], *Kvalstad et al*. [2005], *Laberg and Camerlenghi* [2008], and *Leynaud et al*. [2009]; nevertheless, the actual factors contributing to failure or setting off the instability are often difficult to assess.

The extensive and multidisciplinary slope stability investigations with respect to the safe development of a major gas field (Ormen Lange), within the slide scar of the giant Storegga Slide (off Norway) revealed several important aspects that help to explain the architecture, size, and evolution of the landslide. These include (i) the interplay of glacial and ocean current controlled cyclic sedimentation processes, (ii) lateral fluid migration processes in response to glacial loading, and (iii) the specific geotechnical behavior of so-called "weak sediment layers" [*Bryn et al*., 2003; *Laberg and Camerlenghi*, 2008; *Locat et al*., 2014], with (iv) a high-magnitude seismic event as the ultimate trigger. However, specific conditions apply for different landslides and geological settings, controlled by the regional physiographic and seismotectonic setting.

Weak sediment layers often play a major role in the development of landslides, both offshore and onshore. These layers are defined as sediment layers that have a strength sufficiently lower than that of the adjacent units and therefore provide a potential focus for the initial development of a surface of rupture [*Locat et al*., 2014]. Weak layers in the marine environment are often linked directly to sediments showing some level of stratification, which can cover quite large areas (few hundreds of square kilometers) [*Kvalstad et al*., 2005]. Weak layers within soil and rock slides on land are often controlled by a bedding plane or discontinuity within the stratigraphy [e.g., *Hungr et al*., 2014], and the role of weak layers are well known from studies of snow avalanches [*Föhn et al*., 1998].

In many cases, the failure surface over which the failed sediments move develops at the base of a weak layer and thus follows stratigraphic horizons that are identified on seismic lines by high-amplitude reflections. These horizons are referred to as glide planes (also known as failure planes or slip planes) and are a common feature in several areas with documented mass movements, irrespective of their dimensions [e.g., *Huvenne et al*., 2002; *Bryn et al*., 2003; *Haflidason et al*., 2003; *Laberg et al*., 2003; *Canals et al*., 2004; *Lindberg et al*., 2004; *Bryn et al*., 2005; *Dan et al*., 2007; *Laberg and Camerlenghi*, 2008; *L'Heureux et al*., 2012; *Lucchi et al*., 2012; *Rebesco et al*., 2012; *Rise et al*., 2012]. On the formerly glaciated Norwegian-Barents Sea-Svalbard margin, glide planes typically occur within contouritic sediments [e.g., *Laberg et al*., 2001, 2003; *Bryn et al*., 2003; *Lindberg et al*., 2004]. In the Adriatic Sea, intervals of condensed intervals of mud (maximum flooding surfaces) occur at the base of deformed sediments [*Trincardi et al*., 2004], while in a similar setting of Western Greece, the development of glide planes is related to muddy and gas charged sediments [*Lykousis et al*., 2009].

Weak sediment layers and glide planes are of global concern and need to be investigated as few detailed studies have been undertaken, and thus, their sedimentology and physical properties are not well understood. This is mainly because these layers are remolded and reworked in areas where landslides have occurred. It is furthermore not known how one can unambiguously identify weak layers before failure takes place [*Masson et al*., 2010]. Explaining the nature of a weak layer and glide plane requires sediment cores or boreholes from which samples can be taken for advanced geotechnical and geological analyses. However, these samples are only rarely collected because these layers are often located too deep for conventional coring techniques. It is important not only to know the geotechnical properties of weak layers but also to characterize the geological and physical properties in order to be able to recognize these weaker layers within undisturbed sections. It is, therefore, very important to combine a variety of techniques that will allow a proper integration between the different principles (e.g., sedimentology, geophysics, and geotechnics) to yield information that can subsequently be used in other areas [e.g., *Vanneste et al*., 2013].

The continental slope off the Lofoten Islands, northern Norway, northeast of the Trænadjupet Slide is characterized by the presence of a mass movement complex (Figure 1) [*Bugge*, 1983; *Kenyon*, 1987; *Yoon et al*., 1991; *Baeten et al*., 2013]. This area, in which the bed sediment is largely dominated by contouritic deposits [*Laberg et al*., 1999; *Laberg and Vorren*, 2004], is particularly important, considering that it may be opened for hydrocarbon exploration in the near future [*Rise et al*., 2012; *L'Heureux et al*., 2013].

Baeten et al. [2013] investigated the morphology in the area in detail using swath bathymetry and side-scan sonar data, in order to explain the heterogeneity of smaller-scale mass movements. This study builds upon that work by investigating the stability of the continental slope. To this end, we integrate swath bathymetry, side-scan sonar, and subbottom profiler data, as well as multiproxy analyses of a sediment core that penetrates one of these smaller-scale mass movements and the glide plane. The objectives of this study are to (1) identify and characterize the glide plane and the so-called weaker sediments in which movement was initiated, (2) to link these to the sedimentary processes and paleoenvironments that prevailed during their formation, (3) to use our geotechnical test results to evaluate the present-day stability of the continental slope and to test the

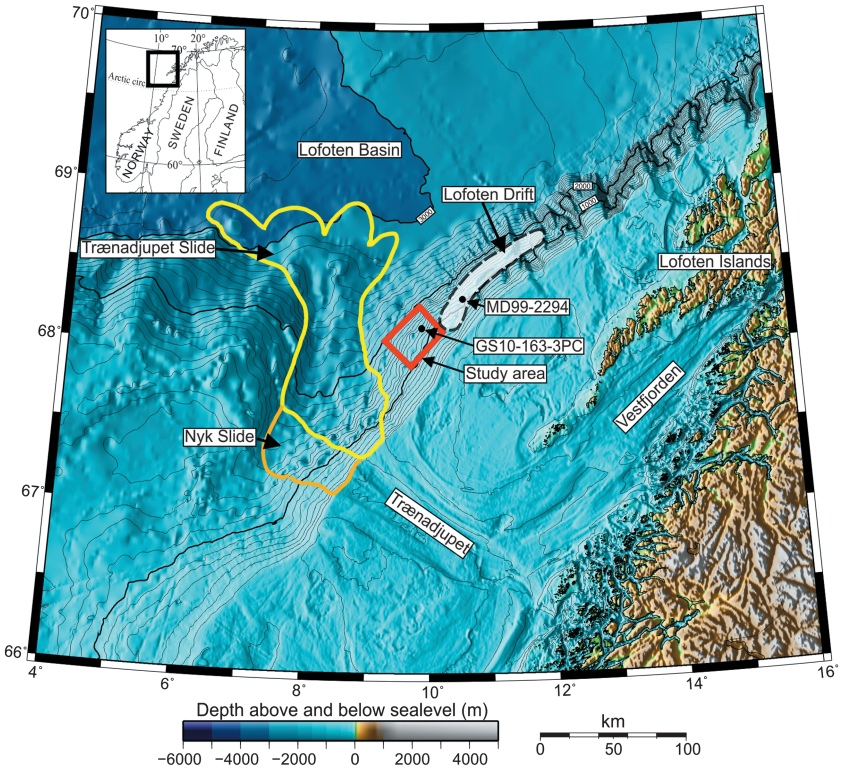

Figure 1. Location map (inset) and bathymetric map of the continental slope offshore the Lofoten Islands, northern Norway, using IBCAO version 3.0 [*Jakobsson et al.*, 2012]. The study area is outlined by the red box, and the location of cores GS10-163-3PC and nearby core MD99-2294 are indicated with black dots. Location of the Nyk and Trænadjupet slides are taken from *Lindberg et al.* [2004] and *Laberg et al.* [2002] and of the Lofoten drift from *Laberg and Vorren* [2004].

inferred mass movements processes by modeling, and (4) to elucidate the preconditioning factors and triggering of the mass movements in this area including the role of the weak layer.

2. Physiographic Setting

2.1. Study Area and Bathymetry

The study area is located on the continental slope off the Lofoten Islands, northern Norway (Figure 1), in water depths between 300 and 2500 m. The shelf edge (at approximately 240 m water depth) lies approximately 100 km off the Lofoten Islands. Compared to other segments of the Norwegian margin, the continental slope is relatively steep (around 5°) in this area [*Vorren et al.*, 1998]. At the base of the slope in approximately 2800 m water depth, a marked reduction in slope angle to about 1° leads to the 3200 m deep Lofoten Basin (Figure 1).

2.2. Ocean Circulation

The Norwegian Current dominates the present-day surface circulation pattern transporting Atlantic Water along the Norwegian continental margin toward the northeast [*Poulain et al.*, 1996]. Artic Intermediate Water flows northeastward along the slope, at a depth of about 800 m west of the Lofoten Islands [*Blindheim*, 1990]. This water mass is presumably responsible for the deposition and modification of the Lofoten Drift from suspended sediments derived from winnowing on the continental shelf and upper slope [*Laberg et al.*, 2001]. Norwegian Sea Deep Water flows below 2000 m in the Lofoten Basin. It enters the area from the northwest across the mid-ocean ridge north of Jan Mayen [*Swift and Koltermann*, 1988].

2.3. Late Weichselian Glacial History

The onset of the late Weichselian glaciation started around 35 cal years ka B.P. (thousands of calendar years before present) [*Andersen*, 1975; *Lauritzen*, 1991; *Olsen et al.*, 2001] and the Fennoscandian Ice Sheet reached the shelf break south of the study area at c. 26 cal years ka B.P. (22 ^{14}C ka B.P.) [*Baumann et al.*, 1995; *Dahlgren and Vorren*, 2003]. The Last Glacial Maximum (LGM), representing the largest global ice sheet volume,

occurred at 21 cal years ka B.P. [*Mix et al*., 2001]. Most probably, the ice front oscillated a few times between 26 cal years ka B.P. and the final deglaciation of the outer continental shelf [*Dahlgren and Vorren*, 2003; *Rørvik et al*., 2010; *Vorren et al*., 2013].

On the outer middle and southern Norwegian shelf (south of the study area), the rapid retreat of the Fennoscandian Ice sheet from the shelf break started between circa 19 cal years ka B.P. (16.5 ^{14}C ka B.P.) [*Dahlgren and Vorren*, 2003; *Laberg et al*., 2007] and circa 17.5 cal years ka B.P. (15 ^{14}C ka B.P.) [*Lehman et al*., 1991; *Hjelstuen et al*., 2004]. The final drawdown and breakup of the Andfjorden ice stream to the north of the study area commenced around 17.8 cal years ka, after a period of downmelting [*Vorren et al*., 2013]. Since the LGM, the continental slope has been affected by both along-slope flowing ocean currents [*Laberg et al*., 1999; *Laberg and Vorren*, 2004] and resedimentation processes.

2.4. Along-Slope Sediment Transport and Deposition

Along-slope currents cause erosion, sediment transport, and deposition on the outer shelf and upper slope. Extensive contourite drifts developed further downslope, for example, the active Lofoten Drift on the continental slope northeast of the study area (Figure 1) [*Laberg et al*., 1999, 2001; *Laberg and Vorren*, 2004]. The Lofoten Drift is actually larger than previously assumed and the southern part of it extends into the study area [*Baeten et al*., 2013].

The sediment composition of the upper part (~24 m) of the Lofoten Drift is relatively uniform and dominated by clay (50–60%) and silt (30–40%) [*Laberg and Vorren*, 2004]. The sedimentation pattern includes alternations of homogeneous and laminated sequences. The homogeneous intervals are interpreted as contouritic muds (silty clays), whereas the laminated intervals represent plumites from meltwater plumes released from the Fennoscandian Ice Sheet [*Rørvik et al*., 2010]. Minor fractions of sand occur dispersed in the mud matrix and/or in lamina or layers. The sand is interpreted to be ice-rafted debris. Differences in the accumulation of the sand are possibly related to variations in iceberg fluxes [*Rørvik et al*., 2010]. The growth of the contourite drift is clearly climatically controlled as sedimentation rates were an order of magnitude higher during the last glacial period compared to the present interglacial period. The uppermost ~10 m of the drift were deposited during the last 20 ka [*Laberg and Vorren*, 2004; *Rørvik et al*., 2010].

2.5. Mass Movements

Two large submarine landslides, the Trænadjupet Slide and the Nyk Slide, are located immediately southwest of the study area (Figure 1). The Trænadjupet Slide removed up to 160 m of glacigenic sediments deposited during the LGM as well as part of the underlying Nyk Contourite Drift (~20 m) [*Laberg et al*., 2003]. The Trænadjupet Slide occurred immediately prior to circa 4.6 cal years ka B.P. (4 ^{14}C ka B.P.) [*Laberg and Vorren*, 2000; *Laberg et al*., 2002]. The older Nyk Slide has a minimum age of about 19 cal years ka B.P. (16 ^{14}C ka B.P.) [*Lindberg et al*., 2004]. The sidewalls of the Trænadjupet landslide lie directly downslope of the area under investigation (Figure 1). The presence of several sandy turbidites in the Lofoten Basin, two of which are correlated with the Trænadjupet and Nyk Slides, indicates repeated large-scale instability in this area [*Laberg et al*., 2006; *Haflidason et al*., 2007].

3. Data and Methods

3.1. Acoustic Data

The side-scan sonar data were collected with R/V *Professor Logachev* in 2008 using a MAK 1 M deep-towed hydroacoustic system operated at 30 kHz with a swath range of up to 2 km. The sonar was towed at a nearly constant altitude of about 100 m above the seafloor at a speed of 1.5–2 knots. The side-scan sonar has a variable resolution of about 7 m to 1 m across track (maximum range to center) and along track (center to maximum range). Onboard data processing included time-variant gain to compensate the recorded amplitudes for the irregularity of the directional pattern of the transducers as well as for spherical divergence. Here we present high backscatter values as light tones, and low backscatter values as dark tones.

Subbottom profiler data (5 kHz) were acquired synchronously with the side-scan sonar data. Under ideal circumstances, the vertical resolution of the subbottom profiler data is about 10 cm and penetration is between 30 and 60 m.

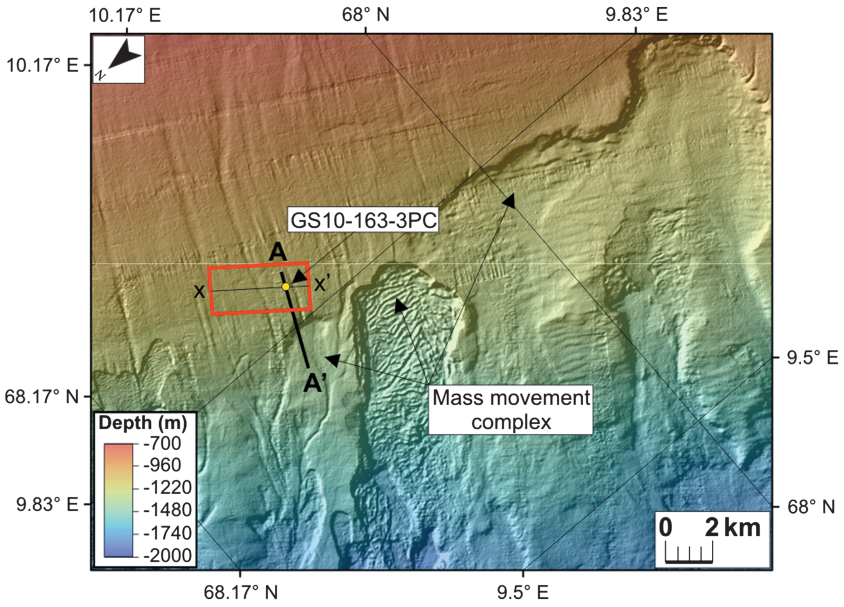

Figure 2. Bathymetic map of the study area. The location of the side-scan sonar data is outlined in red. The subbottom profiler line (x-x') is indicated in black (see Figure 3). The core location is indicated by the yellow circle, and the profile used in the BING model (A-A') is indicated by the black bold line. Note that the data set is rotated (see north arrow).

Most of the swath bathymetry data were acquired with R/V *Jan Mayen* (now R/V *Helmer Hanssen*) in June 2010 using a hull-mounted Kongsberg Simrad EM 300 multibeam echosounder. Additional bathymetric data were provided by the Norwegian Deep Water project SEABED. The two data sets have a 25 m by 25 m grid size and were merged using the Generic Mapping Tools software [*Wessel and Smith*, 1998]. ArcGIS software was used to visualize the data (Figure 2).

3.2. Lithological Data

The 16 m long Calypso core (giant piston core) GS10-163-3PC (68°05.0978'N, 09°52.1969'E, 1178 m water depth) was retrieved with R/V *G.O. Sars* in June 2010 (Figures 2 and 3).

3.2.1. Physical Properties

Prior to opening, bulk density, *P* wave velocity, and magnetic susceptibility of the sediments were measured at 5 mm intervals using a GEOTEK multisensor core logger (MSCL). The MSCL density log was later calibrated with the density values calculated from water content measured of 5 cm^3 sediment samples. After opening, color images were acquired with a Jai L-107CC 3 CCD RGB Line Scan Camera installed on an Avaatech XRF core scanner.

3.2.2. CT Scans/X-Radiographs

Both three-dimensional computed tomography (CT) scans and X-ray images were taken throughout the core to identify the different lithofacies and accurately target specific intervals for advanced geotechnical tests. Whole-core CT scans were taken of all the sections, and some high-resolution 3-D CT scans were taken of the core intervals used for geotechnical analysis afterward (sections J, H, G, and D), using a Nikon Metrology produced model XT H 225 LC industrial type CT scanner with micrometer resolution. Conventional X-radiographs of the remaining sections were taken from split cores.

3.2.3. Logging

Sediment structure and texture were described from split cores, and the colors were determined using the Munsell Soil Color Chart. One centimeter thick samples were sieved for grain-size distribution analysis. The sampling depths were based on the lithological variations within the core, but typically, samples were taken at 20 cm intervals. The samples were wet sieved using the following sieves: 0.063 mm, 0.125 mm, 1.0 mm, and 2.0 mm. Material finer than 0.063 mm was further analyzed with a Micrometrics Sedigraph 5100 in order to separate the silt and clay fractions.

3.2.4. Dating

Ten accelerator mass spectrometry radiocarbon dates on foraminifera (*Neoglogoquadrina pachyderma sinistral*) and one shell fragment provide the chronology for this study. The samples were analyzed at the

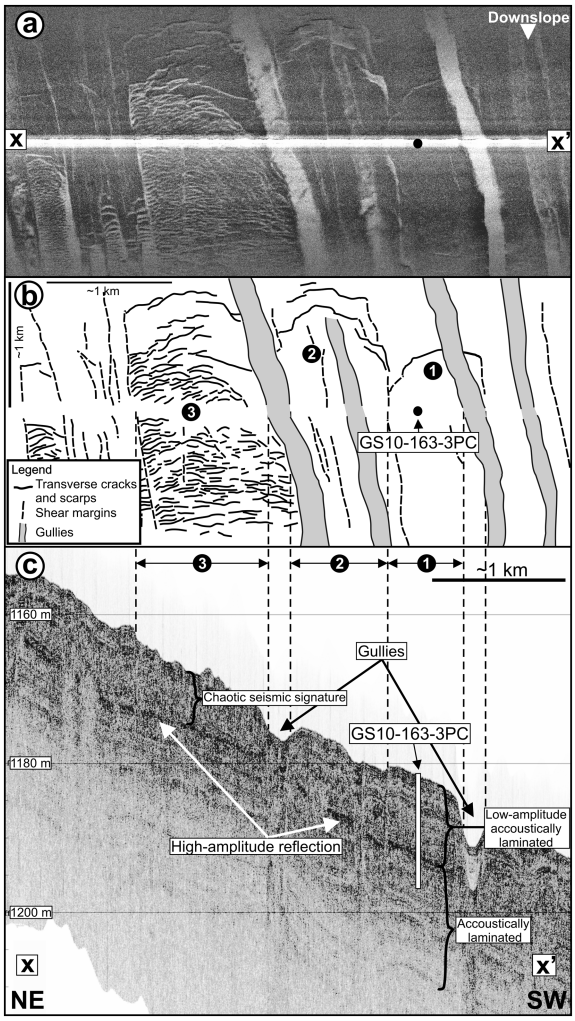

Figure 3. (a) The side-scan sonar data (for location see Figure 2); high backscatter values are presented as light tones and low backscatter values as dark tones. (b) The interpretation of the side-scan sonar data, the black encircled numbers refer to different phases of slide development, see text for further description. (c) The subbottom profiler acoustic data. The location of core GS10-163-3PC is indicated.

Poznan Radiocarbon Laboratory, Poland. The radiocarbon ages were calibrated using the software Calib Rev. 6.0 [*Stuiver and Reimer*, 1993]. The calibration data set used was Marine09.14c [*Reimer et al*., 2009]. A reservoir age of 400 years, and a ΔR of 300 ± 100 years [following *Rørvik et al*., 2010] were applied.

3.2.5. Geotechnical Analysis

Geotechnical tests were carried out at the Norwegian Geotechnical Institute (NGI) on four selected depth intervals in order to characterize the different lithofacies identified on the X-ray and CT images: (i) 6.6–7.1 m depth (section J), (ii) 8.5–8.8 m (section H), (iii) 9.6–9.9 m (section G), and (iv) 12.5–12.8 (section D; Figure 4). Geotechnical tests included index tests (water content, i.e., the ratio of mass of water and the mass of solids in the soil), Atterberg limits (plastic and liquit limits; plasticity index, i.e., the difference between the liquid and plastic limits; liquidity index, i.e., the difference between natural water content and the plastic limit, divided by the plasticity index) and sensitivity (ratio of undrained shear strength in undisturbed and remolded conditions) based on fall cone strength tests on undisturbed and remolded cohesive samples, direct simple shear tests, anisotropically consolidated triaxial tests in compression, and constant rate-of-strain oedometer test (only main phase of loading, thus no unloading or recompression). Prior to the advanced shear tests, the samples were consolidated back to the assumed in situ stress level. The remaining sections were analyzed in the laboratory in Tromsø, focusing on water content and undisturbed/remolded shear strength of the sediments using the fall cone test. All geotechnical tests were performed according to state-of-the-art practice and international standards.

The effective vertical stress (σ'_{v0}) was determined from the MSCL wet-bulk density, assuming normally consolidated conditions (confirmed from oedometer tests), after calibration of the former with laboratory measurements. For normally consolidated cohesive sediments, the ratio of shear strength and effective vertical stress (s_u/σ'_{v0}) is from 0.2 to 0.3. The preconsolidation stress, p_c', was estimated using either the *Casagrande* [1936] method (sample at 12.95 m below seafloor (bsf)) or empirical relationships between undrained shear strength, s_u, plasticity index, I_p, σ'_{v0}, and p_c' [*Lunne et al*., 1997, and references therein] (all other oedometer results). The latter method was the most reliable for the samples retrieved. We also used the advanced geotechnical tests (oedometer, triaxial tests) to assess the sample quality, which appeared relatively poor. Poor sample quality is not uncommon for soft sediments collected with a piston corer, and it is taken into account in further analyses.

3.2.6. Synthetic Seismogram

A synthetic seismogram was created using the *P* wave velocity and wet-bulk density logs from the MSCL. The data were filtered to remove outliers, prior to calculating the acoustic impedance for each slice (0.5 cm thick). Reflectivity at each depth interval is the ratio of the difference and the sum of the acoustic impedances above

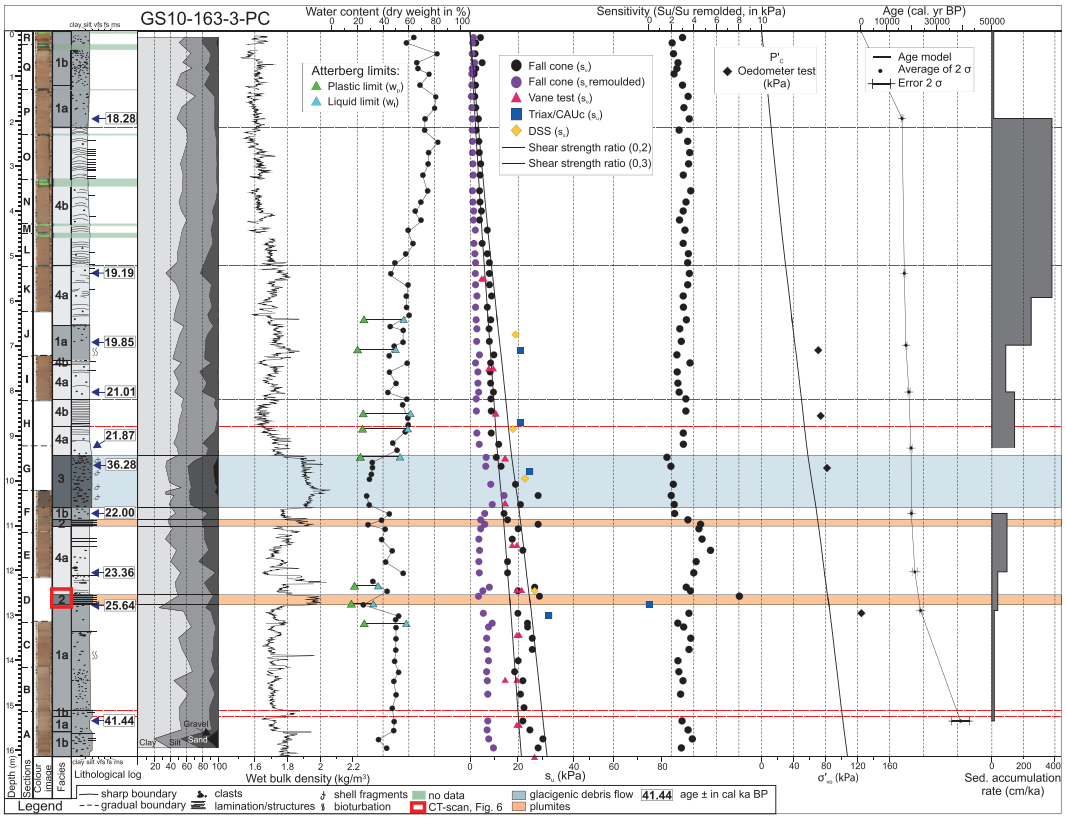

Figure 4. Lithostratigraphy, chronology, and physical properties of core GS10-163-3PC including: (1) The core sections; (2) color images of the core (except from the intervals used for geotechnical analysis); (3) the lithofacies of the core; (4) the lithological core log; (5) the ^{14}C accelerator mass spectrometry (AMS) dates; (6) the grain-size distribution; (7) the wet-bulk density; (8) the geotechnical results, including the water content, the Atterberg limits, the shear strength (based on fall cone strength tests, vane shear tests, triaxial tests, and direct simple shear tests), together with the shear strength ratio from 0.2 to 0.3, the sensitivity, and the oedometer results together with the calculated effective vertical stress (solid line); (9) the age model (based on nine radiocarbon dates); and (10) the sediment accumulation rates.

and below the interval. The *P* wave velocity log was then used to convert depth to time, before resampling the data to match the sampling rate of the wavelet (100 kHz). For the latter, we lacked information from the subbottom profiler data (except the central frequency) and therefore selected a 5 kHz Ricker wavelet as source signature. The convolution of the wavelet with the reflectivity function then yields the synthetic trace. We then also calculated the amplitude envelope as a seismic attribute.

Correlation of the synthetic seismogram and the subbottom profiler acoustic data indicates that the core was stretched (or oversampled) ~14% during recovery. Stretching often occurs in long piston cores, especially in the upper part. Although stretching does not severely affect lithological and physical properties [*Auffret et al.*, 2002; *Széréméta et al.*, 2004], it may affect the geotechnical properties.

3.3. Slope Stability and Landslide Dynamics

In order to evaluate the stability of the continental slope within the study area, we used three different models: (1) the infinite slope model, (2) the BING model [*Imran et al.*, 2001], and (3) the retrogressive slide model [*Kvalstad et al.*, 2005].

In infinite slope equilibrium, the Factor of Safety (FoS) is defined as the shear strength (s_u) divided by the shear stress (τ):

$$\mathrm{FoS} = \frac{Su}{\tau} = \frac{Su}{\gamma' z \sin\alpha \cos\alpha} \quad (1)$$

In this equation, γ' is the submerged unit weight, z is the depth below seafloor to the slip surface, and α is the slope angle. A slope is considered stable when FoS > 1 and unstable when FoS <1. In this simple model,

the shear strength is constant along the slip surface, and no specific rheology can be used. Properties like mass flow dynamics, runout, and spreading cannot be determined.

The debris flow model BING [*Imran et al.*, 2001] is a time-dependent model that adopts the depth-integrated momentum and continuity equations to calculate the movement of a simulated debris flow. Contrary to the infinite slope model, BING can use different rheological soil models (e.g., Bingham, Herschel-Bulkley). In this study, we selected the Herschel-Bulkley model, as it allows a better approximation to the observed viscoplastic behavior of marine clays in laboratory tests run at varying strain rates. The viscoplastic Herschel-Bulkley rheology adopts the relationship

$$\tau = \tau_y + K\gamma^n \tag{2}$$

where τ is the flow resistance, τ_y the yield strength, γ is the strain rate, and n is the Herschel-Bulkley exponent. K is the viscosity parameter. The reference strain rate γ_r is defined as

$$\gamma_r = \left(\frac{\tau_y}{K}\right)^{\frac{1}{n}} \tag{3}$$

The debris mass has an initial parabolic shape with a maximum thickness, a start coordinate, and an initial length. The debris is draped on a specified topographic profile (bedfile). After failure, the viscoplastic debris material flows downslope along the specified slip surface. Strength properties are not allowed to vary with depth in BING; however, the model returns information on flow velocities and run out, but lateral spread is not accounted for.

Kvalstad et al. [2005] developed a retrogressive slide-block model that can explain the Storegga landslide geomorphology and is applicable to other landslides as well. This mechanical model takes into account the strain-softening behavior typical for marine clays for a series of retrogressive slide steps and can also include the effects of excess pore pressure (e.g., due to rapid sedimentation). In this model, deformation takes place incrementally in small steps, conserving total energy. Prerequisites are that the sediments are moderately sensitive (which is typically the case for marine clays), and the unloading caused by one step in the landslide process is sufficient to generate progressive spreading of shear bands due to undrained lateral expansion of the soil, with strain softening in the basal failure plane causing back stepping [*Kvalstad et al.*, 2005]. As such, it is the unloading of the headwall which causes concentration of strain and loss of strength in the base layer, thereby reducing the factor of safety to values below 1 and thus initiating a dynamic landslide evolution process [*Kvalstad et al.*, 2005].

During the failure process, the changes in geometry, volumes, and shear strength are updated and accounted for in the energy balance allowing velocities to be calculated.

As long as excess kinetic energy is produced, the slide mass will accelerate, otherwise the slide block will slow down. Motion will continue until the consumed energy equals the released potential energy [*Kvalstad et al.*, 2005]. This retrogressive model is more advanced than the models discussed above and allows obtaining information on the mass flow dynamics, runout as well as upslope retrogression (back stepping). In addition, it uses site-specific geotechnical parameters as input (e.g., shear strength variation with depth in undisturbed and remolded condition, sensitivity).

The retrogressive slide model simulates the same physical processes as the BING model, but it is formulated differently. The BING model uses a depth-averaged yield strength. By contrast, in the retrogressive slide model, the spreading and breakup of the failing sediment into blocks is included, and the strength increases with depth (both undisturbed and remolded conditions). Both models return essential information for hazard assessment, like energy budgets, flow velocity, and runout distance.

None of the models take hydroplaning into account. Considering the short runouts documented here, there is little reason to believe that hydroplaning plays a significant role in the runouts for the instabilities in the study area.

4. Results and Interpretations

4.1. Shallow Mass Wasting

A mass movement complex is shown on the swath bathymetry data in Figure 2. This mass movement complex is characterized by different styles and sizes of mass movements (2.1–8.7 km^3) [*Baeten et al.*, 2013]. These mass movements have a complex geomorphology that is related to multiphase erosion, e.g.,

Table 1. ^{14}C AMS Radiocarbon Dates Obtained From Core GS10-163-3PC[a]

Sample Name	Depth in Core (m)	Dated Material	^{14}C Age (Uncorrected Radiocarbon Year)	(cal years B.P. 2σ)	(cal years B.P.)
Poz-43215	1.95	N. Pachyderma sinistral	15,700 ± 120	18,665–17,912	18,290
Poz-43216	5.39	N. Pachyderma sinistral	16,670 ± 110	19,488–18,896	19,190
Poz-39686	6.98–7.00	N. Pachyderma sinistral	17,370 ± 120	20,270–19,518	19,850
Poz-43217	8.03	N. Pachyderma sinistral	18,320 ± 110	21,489–20,532	21,010
Poz-39687	9.26–9.29	N. Pachyderma sinistral	18,920 ± 140	22,318–21,428	21,870
Poz-39685	9.64–9.68	Macoma Calcarea fragment	32,400 ± 600	37,625–34,928	36,280
Poz-43218	10.73	N. Pachyderma sinistral	19,130 ± 150	22,443–21,560	22,000
Poz-43219	12.05	N. Pachyderma sinistral	20,200 ± 400	24,335–22,377	23,360
Poz-39688	12.88–12.90	N. Pachyderma sinistral	22,100 ± 200	26,255–25,034	25,650
Poz-43221	15.345	N. Pachyderma sinistral	379,00 ± 1,900	44,889–37,997	41,440

[a]Calibrated using Calib Rev. 6.0 [*Stuiver and Reimer*, 1993] using Marine09.14c [*Reimer et al*., 2009], a reservoir age of 400 years and a ΔR of 300 ± 100 [from *Rørvik et al*., 2010]. The table shows the sample name; the depth of the dated core samples; the type of dated material; the uncorrected ^{14}C age; the calibrated calendar year, within the 2σ age interval of highest probability; and the mean age of the calibrated calendar year (rounded to the nearest tenths).

movement along multiple and arcuate escarpments and the exposure of different glide planes. Such a geomorphological pattern is indicative of retrogressive failure, similar to parts of the Storegga landslide [*Baeten et al*., 2013; *Bryn et al*., 2005].

Farther upslope, a secondary mass movement complex with smaller-scale mass movements (~0.06 km^3) was identified from the side-scan sonar data because of its higher resolution (Figures 2 and 3) [*Baeten et al*., 2013].

Here we focus on these smaller-scale mass movements, with a glide plane at about 10 to 15 m bsf, on a slope of around 2–3° (Figures 3a and 3b). They consist of an along-slope series of escarpments, delineating a number of 10–15 m thick sediment slabs of variable dimensions. The sediment slabs can be up to several hundreds of meters wide, and they are sharply delineated by shear margins or escarpments (Figure 3). This style of mass movement is likely the result of short distance displacement above a basal glide plane [*Baeten et al*., 2013].

From the geophysical data, we identify three zones. In zone 1, a distinct fracture or crown crack has formed due to initial movement of a slab of sediments over a very short distance (Figure 3). In zone 2, we observe a distinct pull-apart window, exposing the glide plane over several tens of meters. However, the mobilized slab shows virtually no disintegration or internal deformation. The slab narrows downslope. In zone 3, the pull-apart window upslope is more complex but seems wider. The slab has disintegrated into a number of smaller features, likely extensional ridges and blocks. In contrast to zone 2, the slab becomes gradually wider downslope. The pull-apart windows in zones 2 and 3 are between 150 and 500 m wide. The observations suggest that both zones 2 and 3 are the result of different controls on the landslide dynamics, but they likely developed both from an initial failure similar to the crown crack in zone 1.

The subbottom profiler data shows a high-amplitude, semicontinuous reflection overlying acoustically laminated sediments subparallel to the seabed at approximately 12.5 m depth (Figure 3c). Above this high-amplitude reflection, the seismic signature within zone 1 is acoustically laminated with low-amplitude reflections. A few low-amplitude reflections characterize the zone 2 sediments, whereas zone 3 is characterized by chaotic/disturbed acoustic signatures. This observation matches the evidence from the side-scan sonar data, which indicates that the slab has nearly completely disintegrated in this area. These observations imply that the high-amplitude reflection separates an overlying acoustically laminated to chaotic signature, where the lateral variation reflects the increasing degree of deformation, from a largely undisturbed acoustically laminated interval below. The high-amplitude reflection coincides with the base of the slabs/zone of blocks and therefore most probably represents the basal glide plane.

4.2. Cored Interval

Sediment core GS10-163-3PC targeted the zone 1 slab and penetrated the acoustically laminated ~0.6 km wide sediment slab, as well as the high-amplitude reflection and the upper part of the underlying acoustically laminated interval (Figure 3).

4.2.1. Chronology and Sediment Accumulation Rates

Ten samples were radiocarbon dated (Table 1 and Figure 4). All dates, except one, appear in a normal order with depth and indicate that most of the recovered sediments were deposited during the late Weichselian

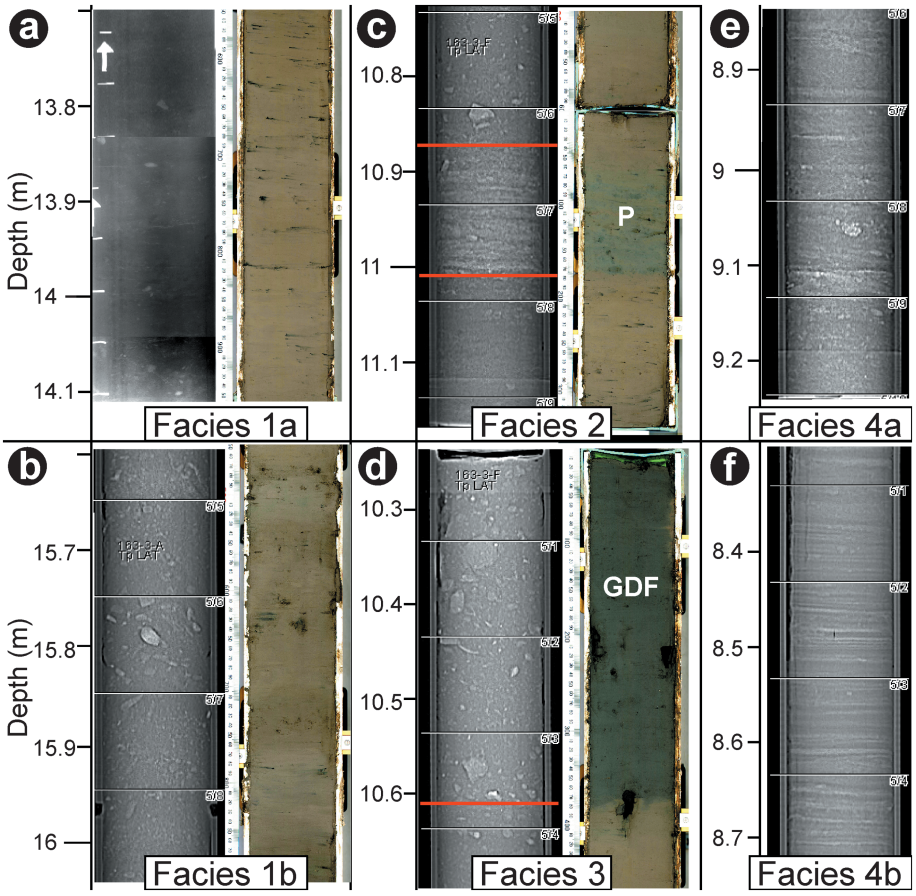

Figure 5. (a) X-radiograph and color image of lithofacies 1a, (b) CT scan and color image of lithofacies 1b, (c) CT scan and color image of facies 2, *P* = plumite, the red lines indicate the facies boundaries. (d) CT scan and color image of facies 3, GDF = glacigenic debris flow deposit, the red line indicates the facies boundary. (e) CT scan of facies 4a. (f) CT scan of facies 4b. The colors of the CT scans have been inverted to make them comparable to the X-radiographs.

(last 40 cal years ka B.P.). The one anomalous date comes from the interval around 9.65 m bsf, which consists of reworked sediments. It was therefore excluded from the age model.

The average sediment accumulation rate was about 16 cm/ka prior to ~26 cal years ka B.P. The accumulation rate increased to about 145 cm/ka between 21.9 and 21 cal years ka B.P., before dropping to 88 cm/ka. The accumulation rate peaked at 380 cm/ka around 18.3 ka cal years B.P. After this peak, the sediment accumulation rate decreased to 12 cm/ka in the upper 2 m of the core (Figure 4). Thus, the average sedimentation rate was highest at the end of the last glacial. This is in agreement with the results of *Rørvik et al*. [2010] suggesting a regional trend for the area.

4.2.2. Lithofacies

The lithofacies 1–4 are defined based on visual descriptions including the grain-size and color of the sediments, structures, and clast content from the CT scans and X-radiographs, and their physical properties (Figure 5 and Table 2). In geotechnical terms, and according to the Norwegian Geotechnical Society, all facies are clays (clay fraction $>$ 30%; Table 2), except facies 2, which is a sandy, silty clay (clay fraction between 15 and 30%). The seismic signature on the subbottom profiler data as well as seismic profiles suggests that the area is dominated by contouritic sediments of the Lofoten Drift which extends into the study area [*Baeten et al*., 2013].

4.2.2.1. Facies 1a

Facies 1a consists of massive greyish brown clay with scattered clasts, some grey silty-sandy lenses/laminae, and some bioturbation (Figures 4 and 5a and Table 2). The boundaries of this facies are mostly gradual. Clasts occur both randomly and concentrated within centimeter thick intervals. This facies is characterized by the largest variations in sediment accumulation rates (12–380 cm/ka) (Figure 4 and Table 2).

Journal of Geophysical Research: Earth Surface

10.1002/2013JF003068

Table 2. Sedimentological, Physical, and Geotechnical Properties of Lithofacies 1–4 in Core GS10-163-3PC[a]

Facies	1a	1b	2	3	4a	4b
Depth within core (m)	15.25–15.59, 12.77–15.12, 6.56–7.33, 1.22–2.15	16.02–15.59, 15.12–15.26, 10.61–10.88, 0.00–1.22	10.88–11.02, 12.54–12.77	9.44–10.61	11.02–12.54, 8.80–9.44, 7.43–8.19, 5.21–6.56	8.19–8.88, 7.33–7.43, 2.15–5.21
Lithology	Massive clay with scattered IRD	Massive clay with IRD	Silty clay with sandy laminae	Massive clay with IRD	Lightly laminated clay	Well laminated clay
Geotechnical soil description	Clay	Clay	Sandy/silty clay	Clay	Clay	Clay
Clasts content	Scattered clasts	High amounts	Scattered clasts	High amounts	Scattered clasts	Relatively low amounts to none
Color (Munsell code)	Greyish brown 2.5Y5/2	Greyish brown 2.5Y5/2	Dark grey 5Y4/1	Very dark grey 2.5Y3/1	Greyish brown 2.5Y5/2	Greyish brown 2.5Y5/2
% clay	43–71	39–67	27–51	34–45	34–56	48–62
% silt	28–47	15–40	42–50	13–34	34–52	33–47
% sand	3–17	9–32	6–19	27–35	3–24	1–16
% gravel	0–1.7	0–15	0–1	1–7	0–2	0–1
Wet-bulk density (kg/m^3)	1.54–1.97	1.51–2.03	1.82–2.01	1.78–2.06	1.59–1.87	1.53–1.77
Magnetic Susceptibility (10^{-5} SI)	10–115	10–145	135–190	70–150	20–135	10–60
Water content (%)	44–80	33–82	24–28	28–32	39–60	49–82
s_u triaxial shear test and direct simple shear test (kPa)	21 (CAUc) 19 (DSS) 33 (CAUc)		75 (*t*)	25 (CAUc) 23 (DSS)	18 (DSS) 27 (DSS)	21 (CAUc)
Plasticity (%)	28.7–32.2		17		18–35	36.5
Sensitivity (kPa)	2.4–3.7	2.0–3.9	4.6–8.1	2.0–3.9	2.5–5.5	2.6–3.7
Sediment accumulation rate (cm/ka)	12–380	12–96	38–96		38–380	96–380
Interpretation	Contouritic/glacimarine	Contouritic/glacimarine	Plumite	GDF	Contouritic/glacimarine	Mainly contouritic
Note	Bioturbated			High content of shell fragments		

[a]Geotechnical soil descriptions are according to the Norwegian Geotechnical Society. GDF = glacigenic debris flow; (CAUc) = anisotropically consolidated undrained triaxial shear test under compression; (DSS) = direct simple shear test.

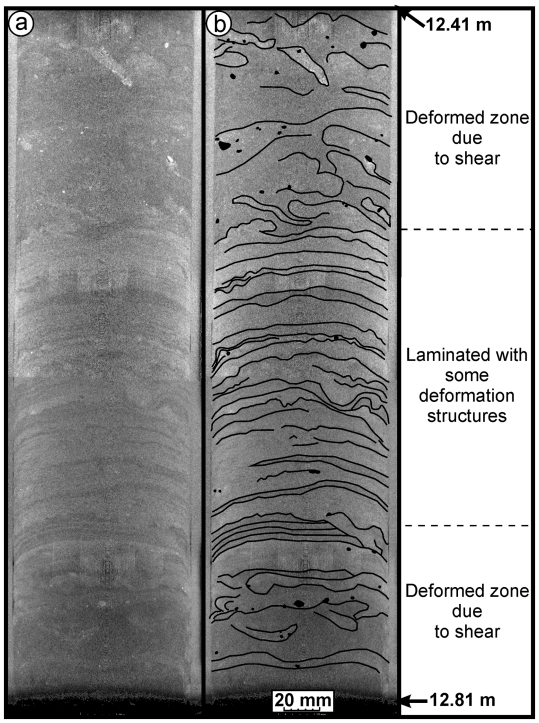

Figure 6. (a) An image from the 3-D high-resolution CT scan of the lowermost plumite interval (12.8–12.41 m depth, outlined in red in Figure 4). (b) Interpretation of the CT scan, showing deformation both above and below the plumite interval.

Facies 1a is inferred to be deposited in an environment dominated by ocean currents, with the clasts being ice-rafted debris, indicating glacimarine conditions. This is in agreement with previous studies [*Laberg and Vorren*, 2004; *Rørvik et al*., 2010]. Variations in sedimentation rate reflect variation in sediment input from the Fennoscandian Ice Sheet and/or fluctuations in flow velocity of the ocean current.

4.2.2.2. Facies 1b

Facies 1b is massive greyish brown clay with high clast contents and some silty-sandy lenses (Figures 4 and 5b and Table 2). The boundaries of this facies are mostly gradual. All intervals of this facies have lower water contents (thus higher wet-bulk density) compared to facies 1a.

In addition to a higher clast content, the sediments in facies 1b are, in general, coarser than those in facies 1a (Table 2). Facies 1b is considered to have the same origin as facies 1a. The higher clast and sand contents indicate a more pronounced glacigenic influence. Facies 1a and 1b represent a subdivision of facies 2 in the nearby core MD99-2294 (for location see Figure 1) [*Laberg and Vorren*, 2004].

4.2.2.3. Facies 2

Facies 2 consists of dark grey silty clay with silty-sandy laminae (Figures 4, 5c, and 6 and Table 2). The laminae have a thickness of a few milimeters to 1 cm. The upper and lower boundaries of this facies are sharp and defined by a change in color, as well as by a change from massive to laminated sediments and vice versa (Figures 5c and 6). Variable, but relatively low water contents and, as a consequence, relatively high wet-bulk density values characterize this facies (Figure 4 and Table 2). This facies occurs in two intervals in the core, (around 11 and 12.7 m bsf). The laminae within the lower of the two intervals show some deformation structures. Levels with irregular to discontinuous laminae indicating deformation occur above and below the interval (Figure 6).

This facies is interpreted as a plumite [e.g., *Hesse et al*., 1997], i.e., a deposit derived from suspension plumes related to meltwater outbursts. Similar deposits occur both south and north of the study area [*Haflidason et al*., 2004; *Lekens et al*., 2005; *Rørvik et al*., 2010; *Lucchi et al*., 2013]. Alternatively, they could have been deposited from turbidity flows. As there is no evidence of an erosional base, we favor the former interpretation.

4.2.2.4. Facies 3

A massive, very dark grey clay with a high content of clasts and shell fragments characterizes Facies 3 (Table 2). It occurs only once throughout the core, between 9.44 and 10.61 m bsf (Figure 4). Whereas the lower boundary is sharp and well defined by a distinct change in color (see Figure 5d), a more gradual change in color characterizes the upper boundary. The shell fragments in the unit belong to species that lived in a cold and shallow water environment, most likely before the LGM.

Because of its basal contact, composition, origin, and the age of the shell fragment, this unit is most likely a glacigenic debris flow deposit.

4.2.2.5. Facies 4a

Facies 4a consists of a slightly laminated greyish brown clay with scattered clasts and some sand lenses/laminae (Figures 4 and 5e and Table 2). Its boundaries are sharp to gradual (Figure 4). The laminae have a thickness of a few milimeters to 1 cm. This facies differs from facies 2 because of its color (dark grey in facies 2), generally finer-grained sediment composition, lower wet-bulk density (thus higher water content), and its more gradual boundaries (Figure 4).

The sediment properties of this facies are similar to facies 1, except for the laminations (Figure 5e and Table 2). This facies is therefore possibly deposited in a similar environment under the influence of ocean currents. Also here, the clasts are likely ice-rafted debris, indicating glacimarine conditions. The lamination can be explained by small variations in current strength along the slope, similar to observations from a nearby core MD99-2294 (Figure 1) [*Laberg and Vorren*, 2004].

4.2.2.6. Facies 4b

Facies 4b consists of a laminated greyish brown clay with scattered clasts and silty-sandy lenses (Figures 4 and 5f and Table 2). Its lower and upper boundaries are gradual. It is generally similar to facies 1 and 4a but is well laminated, finer grained, and has a lower clast content. It also has a comparatively high water content, thus low wet-bulk density. The laminae are 1–5 mm thick and are best observed on X-radiographs, suggesting that they are defined by granulometric changes [see also *Dahlgren and Vorren*, 2003].

This facies is interpreted to have been mainly deposited by along-slope currents. The virtual absence of clasts and sand in this facies indicates a limited glacigenic influence. As in facies 4a, the laminae in facies 4b are thought to be the result of small variations in current strength [see also *Laberg and Vorren*, 2004].

In summary, the cored interval mainly consists of contouritic sediments with a varying influence of glacimarine input, in addition to two plumite intervals and a glacigenic debris flow deposit.

4.2.3. Geotechnical Properties

4.2.3.1. Shear Strength and Sensitivity

In general, the shear strength increases linearly with depth from about 2 kPa at the top of the core to ~30 kPa at its base (Figure 4). Higher shear strength values generally occur within the intervals corresponding to facies 2 (plumite) and 3 (glacigenic debris flow deposit (GDF)). The sensitivity is low within facies 3 (2.0–3.7, typical values for marine clays), but relatively high (4.6–8.1) within facies 2, as well as in parts of facies 4a (2.5–5.5), the latter being located between the two intervals of facies 2. The highest sensitivity of 8.1 occurs within the upper boundary of the lowermost plumite interval (facies 2 at 12.58 m bsf; Figure 4).

4.2.3.2. Plasticity

The plasticity index (I_p), typically ranges between 29 and 37%. There are two exceptions just above and within the lowermost facies 2 interval at 12.35 and 12.75 m bsf (Figure 4) with lower plasticity index values of 17 and 18%, respectively. These two measurements come from intervals with higher bulk densities that contain typically coarser-grained sediments compared to the other samples where the Atterberg limits were measured (Figure 4). The plasticity index is, however, not a critical parameter in the slope stability modeling.

4.2.3.3. Shear Strength Testing Results

In order to facilitate comparison with results from other areas, we normalized the results from the triaxial and direct simple shear tests. Normalization was done by dividing the shear stress by the axial consolidation stress. Note that the triaxial shear test and direct simple shear tests were performed after consolidating the samples to in situ stress levels. The results indicate that some strain softening (i.e., loss of shear resistance with strain after peak strength is reached [see *Kvalstad et al*., 2005]), as well as increasing pore pressure with larger strains, occurs in the samples from 13.0, 9.8, 8.7, and 7.1 m bsf (Figure 7a). However, the strain softening developing up to 15 to 20% shear strain is less than observed in the marine clays that played a dominant role in the Storegga Slide [*Kvalstad et al*., 2005], i.e., with lower brittleness but still higher sensitivity, which could be caused by sample disturbance. The lowermost plumite interval (facies 2; 12.7 m bsf) shows dilative behavior, i.e., a decrease in pore pressure with increasing shear strain (Figure 7b). This unit contains up to 19% sand and up to 50% silt, and is somewhat denser than the sediments above and below. Its undrained shear strength is considerably higher than in the adjacent units. The direct simple shear test at 12.4 m (just above the lowermost plumite interval) shows a continuous increase in pore pressure with increasing strain and shear strength falling in the range typical for marine clays (Figures 7c and 7d).

In summary, the geotechnical analyses yield mainly normal values except for the sediments between 9.44 and 12.77 m bsf. Both plumite intervals and the glacigenic debris flow deposit are geotechnically stronger (Figures 4 and 7), whereas the contouritic sediments with glacimarine influence in between (11.02–12.54) have comparatively high sensitivity values indicating a "weaker" interval.

4.2.3.4. Consolidation

Relatively high shear strength values within facies 2 and 3 fall outside the trends in shear strength ratio for normally consolidated clays ($s_u/\sigma'_{v0} = 0.2–0.3$ and Figure 4). These results suggest that the sediments are

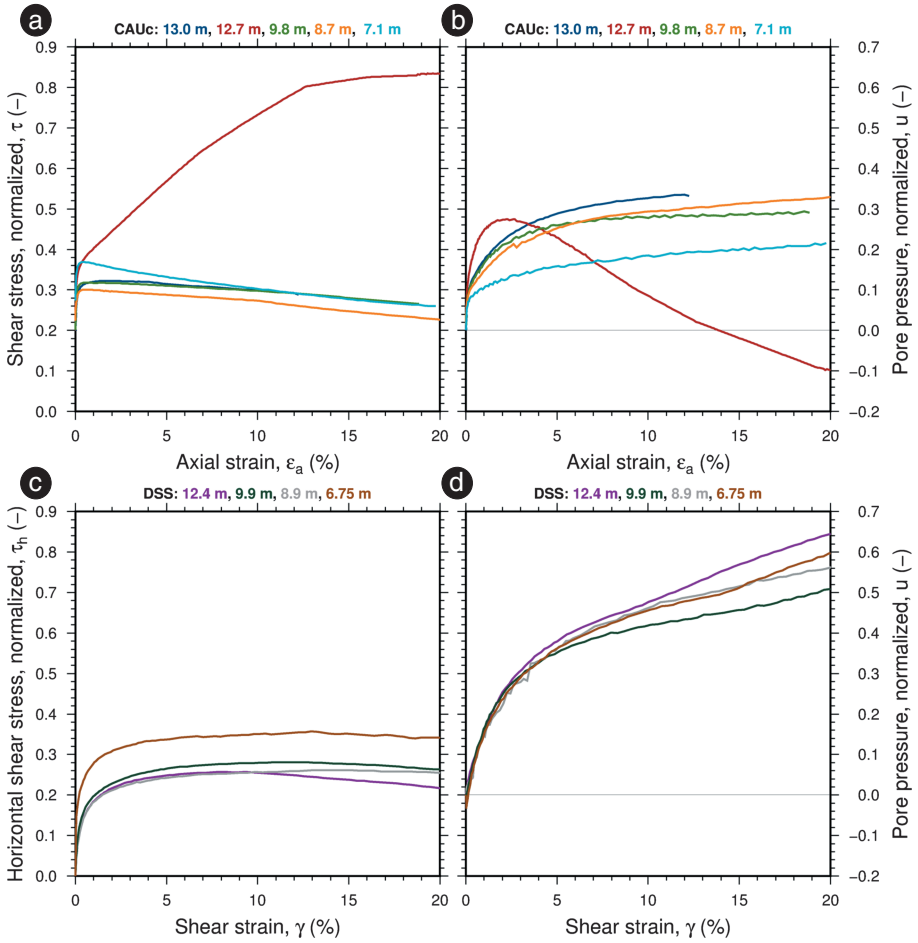

Figure 7. (a) The normalized shear stress values as a function of axial strain from the triaxial shear test. (b) The normalized pore pressure response values as a function of axial strain from the triaxial shear test. Note that the sample from 12.7 m behaves different compared to the other test results, as it dilates. (c) The normalized shear stress values as a function of shear strain from the direct simple shear tests. (d) The normalized pore pressure response as a function of shear strain from the direct simple shear tests. The different colors mark different sample depths at which the respective tests were conducted.

slightly overconsolidated. Figure 4 shows that the measured water contents lie in most cases very close to the liquid limit, an observation which also indicates close to normally consolidated soils.

Data from the odometer tests can be used to estimate the overconsolidation ratios. For these tests, we largely rely on empirical relationships combining plasticity index, shear strength, and in situ stress [*Lunne et al.*, 1997, and references therein]. For the sample at 12.95 m, the results of this empirical method correspond well with the Casagrande method [*Casagrande*, 1936]. The stress history of all four odometer samples indicate that the maximum past stresses (p'_c) acting on these deeper sediments were similar or slightly larger than the present state of effective stress (σ'_{v0}), with ratios between 1.05 and 1.30. Hence, the sediments are normally consolidated to slightly overconsolidated (Figure 4). However, the samples were taken from shallow depths (maximum 12.95 m bsf), and the sample quality observed from the laboratory tests is relatively poor.

4.2.4. Synthetic Seismogram—Correlation of Lithostratigraphy and Seismostratigraphy

We correlate the core with the seismic data through the synthetic seismogram and the amplitude envelope attribute. The strongest reflection on the synthetic seismogram arises at a depth of approximately 12.0–12.9 m (Figure 8). At these depths, we find the highest *P* wave velocity and density values of the lowermost plumite interval in the core (12.54–12.77 m bsf). This depth interval matches the high-amplitude discontinuous reflection on the subbottom profiler data (Figure 9) considered to be the basal glide plane of the slab.

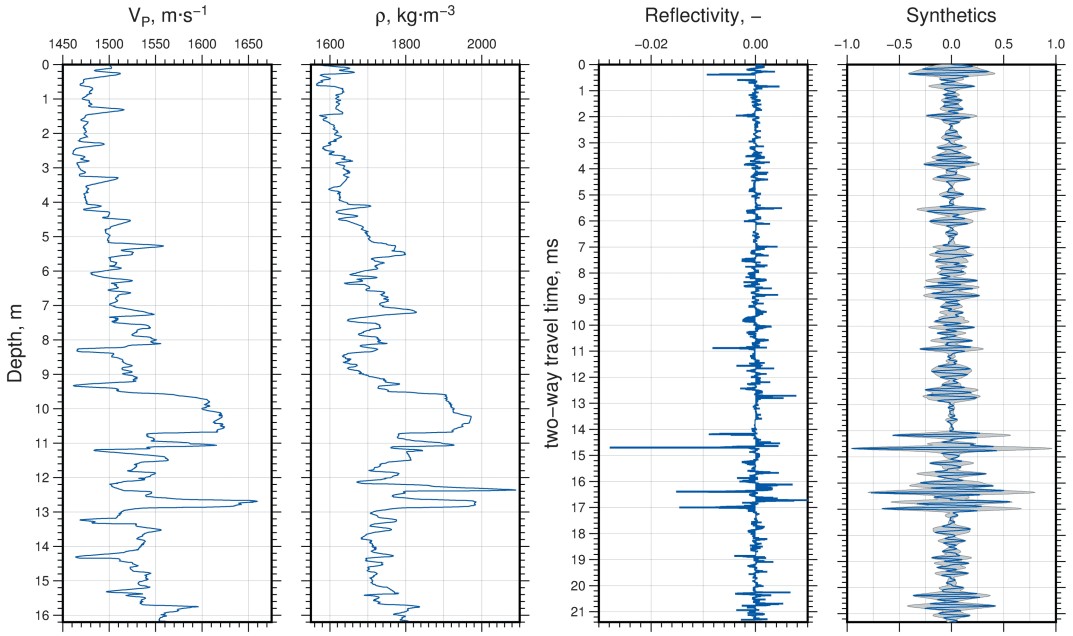

Figure 8. The *P* wave velocity (first column) and bulk density (second column) measured (MSCL) on core GS10-163-3PC. The reflectivity function (third column) is derived from the first and second columns. Finally, the synthetic seismogram (fourth column), with the amplitude envelope in grey is obtained using a 5 kHz Ricker wavelet (not shown) convolved with the reflectivity function (third column).

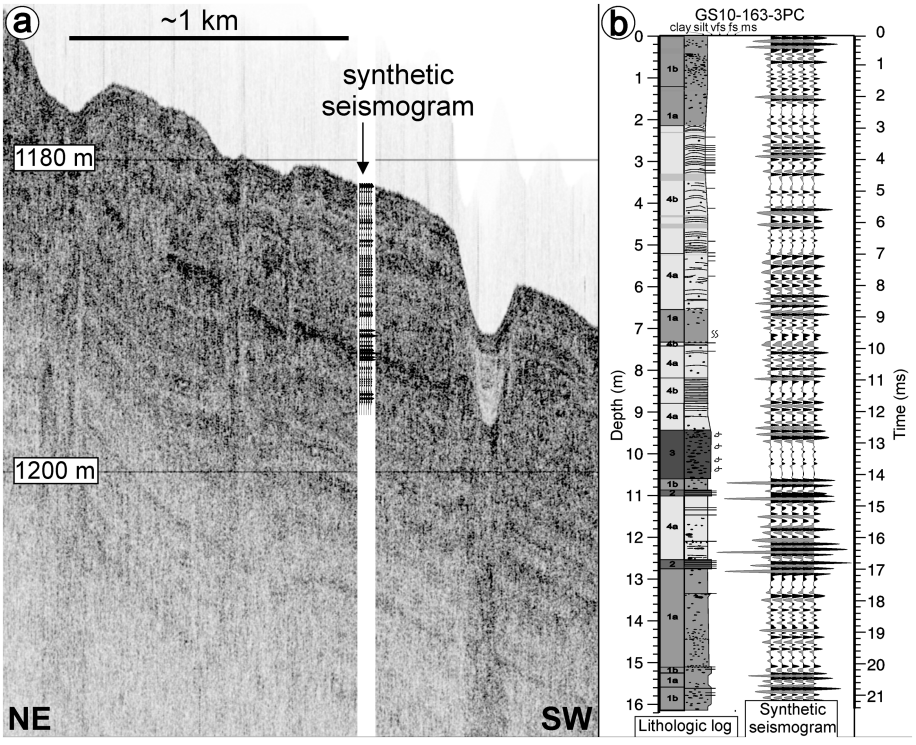

Figure 9. (a) The envelope of the synthetic seismogram plotted within the subbottom profiler data; (b) correlation of the synthetic seismogram with core GS10-163-3PC.

Table 3. Input Parameters for the Modeling

Parameters	Infinite Slope Model	BING Model	Retrogressive Slide Model
Submerged unit weight γ' (kN/m^3)	7.5		7.5
Depth z (m)	12	12	12
Slope angle α (°)	3	2.5	3
Shear strength s_u (kPa)	15.7		
Remolded shear strength at the base $s_{u,rem}$ (kPa)	4.8	4.8	4.8
Depth-averaged yield strength τ_y (kPa)		2.2	
Bulk density, ρ (kg/m^3)		1783	
Herschel-Bulkley exponent n		0.12	
Reference strain rate γ_r		29.3	
Length of deposit (km)		2.5	
Height reduction Δh (m)			6
Frontal wedge angle β (deg)			38
Normalized shear strength α_c			0.325
Sensitivity S_t slide mass			4
Sensitivity S_t slide base			6

4.3. Slope Stability Assessment

As indicated above, we used the sedimentological and geotechnical data as input into three landslide evolution models in order to assess the present-day slope stability and to check if it is numerically possible to back calculate the observed mass movement from our data (Table 3). In addition, the models will also shed light on possible triggering mechanisms and dynamic processes that have played a role in the mass movements in this study.

The parameters used in the models were taken or derived from the geotechnical test results and are summarized in Table 3.

4.3.1. Infinite Slope Model

The geophysical data indicate that the smaller-scale instabilities involve a relatively thin translational sediment slab. The height-to-length ratio therefore approximates an infinite slope, and thus, the infinite slope model can be used to evaluate the FoS and shed light on whether or not external triggers are needed to explain the failure. Using the geotechnical soil data and geophysical data as input (Table 3), we obtain FoS values around 4, i.e., well above 1, which implies that, under present conditions, the slope is stable. When using the remolded shear strength, assuming that movement started by an external trigger, the FoS approaches 1, i.e., it brings the slope close to failure conditions.

These results indicate that an external trigger is necessary to set off the landslides, as the shear strength in the failure plane needs to be degraded to remolded conditions. This simple model does not explain why disintegration may occur or how far the debris may run out, and it is therefore of limited use for hazard assessment.

4.3.2. BING Model

We used the BING model to investigate the debris flows with respect to the topography and geometry and to obtain critical properties, like the frontal flow velocities [e.g., *De Blasio et al*., 2003, 2005; *Issler et al*., 2003, 2005; *Locat et al*., 2004]. The drape used in the BING model represents the slab of sediments from which the core was taken, upslope of the larger landslide complex (see Figures 2 and 3).

In this study, we use an averaged (remolded) yield strength of 2.2 kPa, calculated from the geotechnical measurements at 12 m bsf (Figure 4 and Table 3), within the "weaker" interval characterized by higher sensitivity values (11.2–12.54 m bsf). Figures 10a and 10b show the frontal velocity of the moving mass versus the distance traveled, as well as the displacement of the seafloor for each time interval. The topographic profile used in the model is extracted from the swath bathymetry data. It crosses the core location from upslope the escarpments down to the slide scar immediately downslope (Figures 2 (A-A′) and 10c). For the other parameters used, we refer to Table 3. The sediment drape was 2.5 km long and is situated between 0 and 2500 m (Figure 10c). In this simulation, we use the remolded shear strength, thus implying an external triggering of the failure.

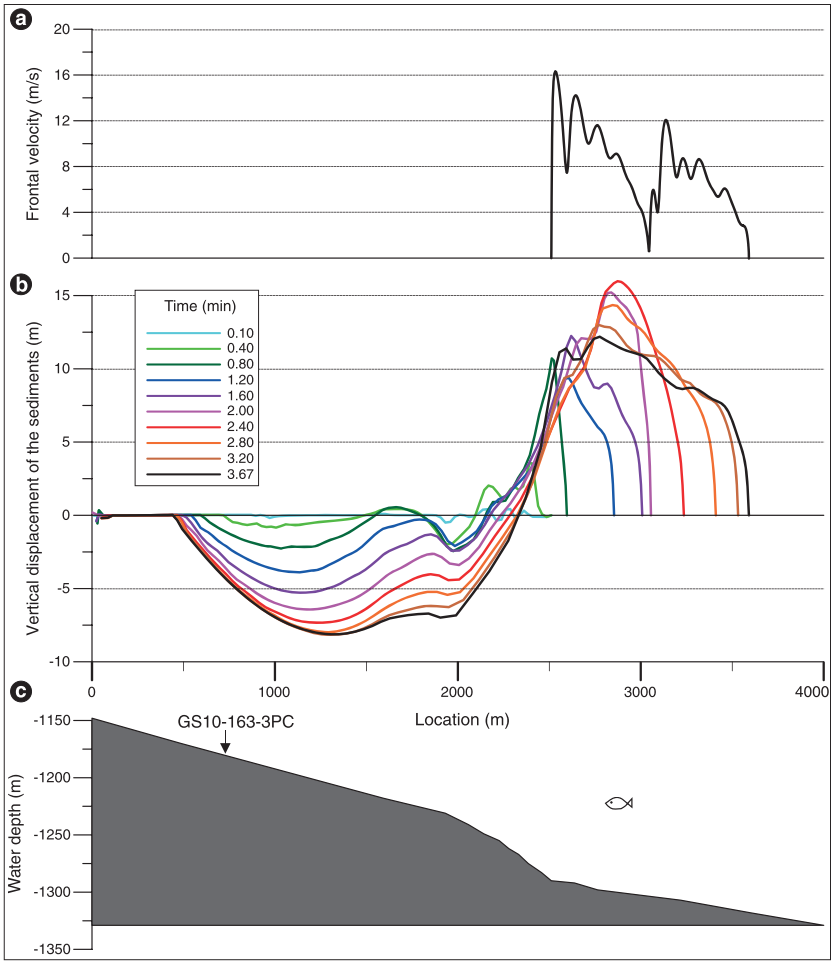

Figure 10. Results obtained from the BING model [*Imran et al.*, 2001]. (a) The frontal velocity versus distance in meters. (b) The colored lines show the displacement of the seafloor for each of the time intervals. The sediment drape is 2.5 km long (between 0 and 2500 on the *x* axis). (c) The bedfile (topographic profile) employed, the profile crosses the location of core GS10-163-3PC (see Figure 2 for location).

The frontal velocity (Figure 10a) is characterized by two similar cycles of a rapid increase, followed by a more gradual decrease. Frontal velocity peaks at about 16 m/s within the first cycle (Figure 10a). The first increase in velocity is because the mass in the lowermost part of the drape fails over the slide scar in the depth profile (Figure 10c). When this mass reaches the slope beyond the slide scar, it slows down to 0.5–1 m/s at approximately 3050 m. The second cycle starts when the mass above the slide scar also starts to move because of undercutting. It then also pushes the first mass farther downslope. The displacement curves (Figure 10b) show the same pattern.

These results show that it is possible to model the mass movements in this study using the BING model and obtain some dynamic properties like the frontal velocities, slide mechanism, and sediment displacement. We realize that the runout distance and velocities calculated are strongly dependent on the input parameters. This is typical for processes changing from stable to unstable conditions and with uncertainty in the parameters (mainly averaged yield strength and viscosity), and how they are transformed during the distortion/remolding process of a slide event.

4.3.3. The Retrogressive Slide Model

The retrogressive slide model was used to model the retrogressive sliding and observed deposition within the Ormen Lange area [*Kvalstad et al.*, 2005]. Even though the mass movements within our study area are smaller, the geophysical data suggest that the same processes are applicable, particularly considering the presence of a distinct slide scar immediately downslope as well as slide blocks and slabs with different

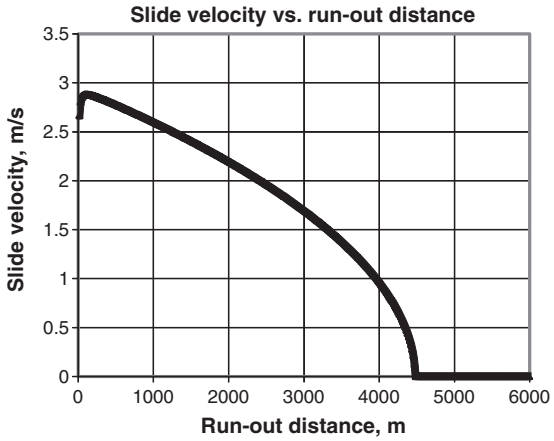

Figure 11. Results obtained from the retrogressive slide model [*Kvalstad et al*., 2005] showing the slide velocity and kinetic energy versus the frontal runout distance.

degrees of deformation (Figure 2). This initial larger-scale failure at the toe of the smaller-scale instabilities (part of the landslide complex in Figure 2) is essential for the retrogressive slide model.

The input parameters for the retrogressive models are primarily geometry, intact, and remolded normalized shear strength and in situ pore pressure conditions (see also Table 3). The geometry is controlled by the stratification and inclination of the basal slip plane and the assumed geometry of the failure model [*Kvalstad et al*., 2005]. In our simulations, we ignored excess pore pressure, as the modest sediment accumulation rates do not give reason to believe that excess pore pressure was generated. In this simulation, remolded shear strength was used, implying an external triggering of the failure.

The retrogressive model predicts a runout of 4.5 km (Figure 11). The retrogressive back stepping from the starting point is also 4.5 km long because the thickness of the debris is set to half the intact thickness. These results fit reasonably well with the observations (Figure 3).

Applying sediment strength parameters from GS10-163-3PC therefore demonstrates that retrogressive failure of the slide masses is a possible and likely slide mechanism for failure along the glide plane, if the mass movement is initiated by an external trigger.

5. Discussion

We first address the depositional environment of the cored interval before turning to the processes of failure of these deposits including the depth and origin of the "weaker sediments" and the basal glide plane. Finally, we discuss the preconditioning factors and triggering mechanisms of the event including the role of the weaker sediments.

5.1. Late Weichselian-Holocene Depositional Environment

Based on the lithology and chronology of the cored sediments, the late Weichselian-Holocene paleoenvironment is divided into four phases:

41.4–25.7 cal years ka B.P. The sediments (facies 1a and 1b) were likely deposited in an glaciomarine environment influenced by ocean currents. The clasts were ice rafted by sea ice and/or icebergs from an ice sheet at the coast (Figures 4 and 12a) that later advanced onto the shelf. The onset of the late Weichselian glaciation in the Vestfjorden area started after 35 cal years ka B.P. [*Andersen*, 1975; *Lauritzen,* 1991; *Olsen et al*., 2001], with the Fennoscandian Ice Sheet reaching the shelf break at circa 26 cal years ka B.P. (22.000 ^{14}C years B.P.) [*Baumann*, *et al*., 1995; *Dahlgren and Vorren*, 2003].

25.7–21.9 cal years ka B.P. The sediments consist of plumites (facies 2), glacigenic debris flows (facies 3), and contouritic sediments (facies 4a). The Fennoscandian Ice Sheet probably extended to the shelf break during most of this period (Figure 12b).

According to *Vorren et al*. [2013] a period with warmer climate occurred around 23.5 cal years ka B.P. on the nearby Andøya. Improved climate conditions may have resulted in ice sheet oscillations on the Lofoten-Vesterålen continental margin. It is likely that these plumites are formed by meltwater plumes caused by oscillations of the ice front. The timing of the plumites also correlates well with laminated sediments and enhanced ice-rafted debris (IRD) fluxes indicating instability of the Fennoscandian ice sheet reaching a maximum between circa 25 and 24 cal years ka B.P. in nearby core MD99-2294 (Figure 1) [*Rørvik et al*., 2010].

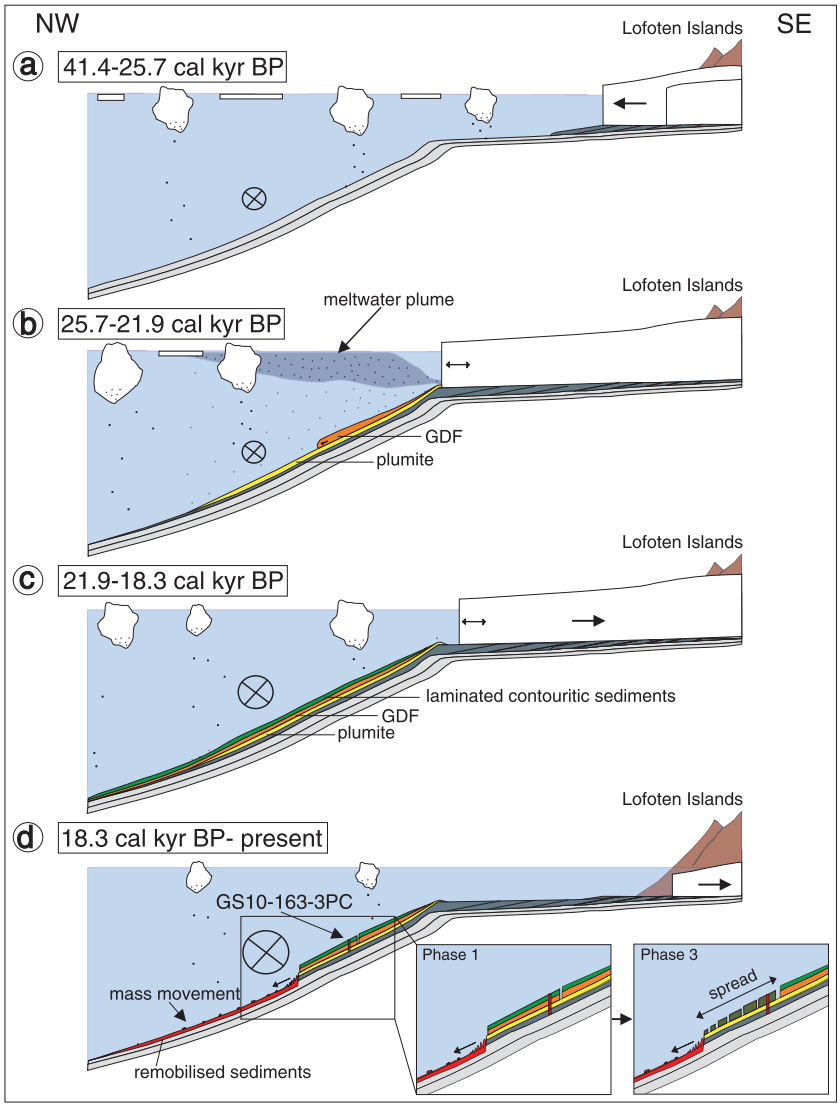

Figure 12. Conceptual model summarizing the sedimentary processes and paleoenvironment of the studied interval on the continental slope offshore northern Norway. (a) Between 41.4 and 25.7 cal years kyr B.P. mainly glaciomarine sedimentation occurred. (b) From 25.7 to 21.9 cal years kyr B.P., plumites, glacigenic debris flows, and contouritic sediment were deposited. (c) Between 21.9 and 18.3 cal years kyr B.P., the study area was dominated by the deposition of contouritic sediments. (d) Between 18.3 cal years kyr B.P. and the present, mainly glaciomarine to marine deposition occurred, together with mass movement in different phases. The circled cross indicates the direction and the strength of the contour current.

The timing of deposition of the plumites in the study area is different to the deposition of other plumites found on the Norwegian-Barents Sea margin by *Lekens et al.* [2005] and *Lucchi et al.* [2013]. The latter were deposited during the early deglaciation by major meltwater release during ice stream retreat [*Lekens et al.*, 2005; *Lucchi et al.*, 2013], while offshore Lofoten they were deposited during the Last Glacial Maximum. Plumites deposited during the LGM have also been reported from the Trinity trough mouth fan (Newfoundland) by *Tripsanas and Piper* [2008].

21.9–18.3 cal years ka B.P. The sediments (facies 1a, 4a, and 4b) were deposited in a glaciomarine environment mainly controlled by ocean currents, with the clasts being ice-rafted debris. The Fennoscandian Ice Sheet was probably oscillating toward the shelf break several times during this period (Figure 12c) [*Rørvik et al.*, 2010; *Vorren et al.*, 2013]. Sediment accumulation rates increase from 250 cm/ka to almost 400 cm/ka at the end of this period (Figure 4). These values are somewhat higher compared to the late Weichselian sedimentation rates of 190 cm/ka calculated from nearby core MD99-2294 (Figure 1) [*Laberg and Vorren*,

2004]. This increase in sediment accumulation rate is most likely caused by increased deposition by bottom currents and input of material toward the end of the LGM.

The sediment accumulations rates dropped to (20 cm/ka) around 18.3 cal years ka B.P., and the sediments changed from being laminated (facies 4b) to finer-grained, massive, more homogenous sediments with more IRD (facies 1a and b; Figure 4). This change may represent the onset of the final deglaciation in the study area and correlates well with results from other studies. It indicates that the final retreat of the Fennoscandian Ice sheet from the shelf break started between circa 19 and 17.5 cal years ka B.P. [*Lehman et al*., 1991; *Dahlgren and Vorren*, 2003; *Hjelstuen et al*., 2004; *Vorren et al*., 2013].

18.3 cal years ka B.P. to the present. The sediments were deposited in a glaciomarine to marine environment influenced by ocean currents with the clasts being ice rafted by icebergs and/or sea ice during the deglaciation of the Fennoscandian ice sheet and during the Holocene (Figure 12d). Sediment accumulation rates were low during this interval (12 cm/ka) and are comparable to rates of 9 cm/ka during the Holocene in nearby core MD99-2294 [*Laberg and Vorren*, 2004]. The reduced sedimentation rates and coarser sediments probably indicate that currents were strong during the last part of the deglaciation as well as in the Holocene and that sediment input was low. The uppermost 30 cm of the core has a different color compared to the sediments below (Figure 4). The change in color is interpreted to take place at the late Weichselian/Holocene boundary, caused by the warmer climatic conditions and the full intrusion of the Norwegian Current at this time [*Vorren et al*., 1984; *Thomsen and Vorren*, 1986; *Hald and Aspeli*, 1997], which most likely caused a change in the biologic productivity within the water masses.

The study area is greatly influenced by the deposition of contourite drifts. The sediments within core GS10-163-3PC show, however, that the depositional environment was more complex than revealed from acoustic data showing a dominantly acoustically laminated signature. Besides contourite drift sediments, glacigenic input from meltwater plumes and debris flows played an important role.

5.2. Processes of Failure and Localization of the Glide Plane

The geomorphology of the area and the shallow mass movement in particular suggests that the failure of the late Weichselian-Holocene deposits started out as a translational slides (Figures 3a and 3b). The mass movement then evolved through spreading of the slab above a glide plane bounded by well-defined lateral shear margins. During downslope displacement, disintegration took place but was highly variable, as evidenced from the side-scan sonar data which shows that in some cases, the slab seemed to have moved without much deformation, whereas a neighboring slab may have been nearly completely disintegrated (Figure 3) [*Baeten et al*., 2013]. This observation may indicate that, whereas similar preconditioning factors apply, the relative strength of the subsurface and overburden control the deformation processes.

In this study, we investigated the movement of this slab in more detail, also in relationship with the landslide complex farther downslope. The variations in the seismic signature on the subbottom profiler data within the blocks clearly reveal varying degrees of deformation in adjacent slabs, related to the different phases in the failure process (Figure 3c). Within the sediments affected by the initial stage of the instability (zone 1), the original acoustic lamination remains virtually intact, and the slab has moved over short distances through deformation within and around the glide plane at the base of the slab. The fact that we do not see deformation within the overlying sediments confirms the hypothesis of slab movement. In zone 2, the sediments within the slab are more disturbed, and within zone 3 a chaotic seismic signature indicates significant deformation and loss of the original stratigraphy, due to either the disintegration of the slab into smaller blocks or partial remolding of the sediments (Figure 3c).

The core was taken within zone 1 (Figure 3), penetrating the slab, as well as the high-amplitude semicontinuous reflection at its base at about ~12.5 m bsf (Figure 3c) that was correlated to the lowermost of the plumite intervals (12.54–12.77 m bsf) (Figures 4, 8, and 9). This plumite has a relatively high wet-bulk density, low water content, high shear strength values, and low plasticity index values. One sample in the upper part of the interval has a higher sensitivity (approximately 8), which does not match the soil characteristics of this particular unit (Figure 4). The triaxial shear test (Figures 7a and 7b) from 12.7 m bsf shows dilative behavior with pore pressure decrease with increasing shear strain and high undrained shear strength. These results make it unlikely that movement started within this interval.

The high-resolution X-radiograph (Figure 6) shows some deformation within the laminated interval, and deformed zones above and below it. This deformation could be related to shear due to movement of the overlying sediment block. This interpretation is supported by the fact that laminations are still visible (Figure 6). Thus, deformation did not take place within the laminated interval, but most likely above it.

Sensitivity values of the contouritic sediments above the plumite interval (11.02–12.54 m bsf) are relatively high (up to 5.5; Figure 4), especially compared to the relatively low values (1.6–4.6) of the overlying plumite (10.88–11.02 m bsf) and the glacigenic debris flow deposit (9.44–10.61 m bsf). Typical sensitivity values for marine clays are around 3 to 5 [*Kvalstad et al*., 2005]. This contourite unit also has high water contents (32–56%) compared to the two plumite intervals (24–28%).

We therefore conclude that movement was most likely initiated within the interval with contouritic sediments between the two plumite intervals (11.02–12.54 m bsf). It stopped on top of the lowermost plumite interval, moving on top of it and resulting in deformation within and around the interval (Figure 6). As the synthetic seismogram linked the top of this plumite interval (12.45–12.77 m bsf) to the high-amplitude reflection on the subbottom profiler data, we can hereby confirm its interpretation as the basal glide plane.

5.3. Preconditioning Factors of Failure

The preconditioning factors often depend on regional geology and local site conditions. The conditions leading to actual failure often form a complex pattern of interacting processes [*Vanneste et al*., 2006]. Below, we will discuss a few factors that have influenced the stability of the sediments on the continental slope in the study area.

5.3.1. Properties of the Contourites and Plumites

The interpretation of our multidisciplinary data set indicates that the critical unit for failure corresponds to sediments characterized by facies 4, sandwiched between the two plumite intervals (11.02–12.54 m bsf). As discussed above, this facies is likely the result of deposition under the influence of contour currents complemented by input from the ice sheet (ice-rafted debris; turbid meltwater runoff). These sediments were deposited when the Fennoscandian Ice Sheet reached its maximum extent. The interface between the 32 cm thick plumite interval (12.45–12.77 m bsf), and the contouritic sediments above is interpreted to have served as the basal glide plane. The plumite interval was deposited during the same period by meltwater plumes.

Glide planes occur often at the interface between sediments with different grain-size compositions and physical/geotechnical properties. Within the study area, the plumites have a high density and shear strength, and a low water content. The combination of the weaker contouritic sediments directly above the stronger plumites has likely influenced on the formation of the glide plane at the contourite-plumite interface and promoted the mass movement. The opposite strength relationship occurs for post LGM plumites in other areas, as a consequence of very high sedimentation rates [*Lekens et al*., 2005; *Lucchi et al*., 2013]. Thus, post-LGM plumites might not have the same effect on the stability of the continental slope.

We speculate that the marked contrast in physical properties at the contourite-plumite interface has also had an influence on the sediment deformation and glide plane development. If correct, both the physical properties of the contourites and the contrast to the underlying plumite deposits may have influenced the slope stability.

In Finneidfjord, *L'Heureux et al*. [2012] identified a stratified event bed consisting of a thin sand unit sandwiched between silty clays. The glide plane was interpreted to be at the interface of the sand below and the silty clay above. On the Vesterålen margin, the slip planes of the mass movements lie within laminated glacial marine clays, overlying a well-defined seismic horizon [*L'Heureux et al*., 2013]. These laminated silty clays have a higher plasticity and water content compared to the surrounding soils (sandy clays), and they exhibit a modest strain-softening behavior in triaxial tests.

Weak layer formation can result from various processes: sedimentological (e.g., layering), geotechnical (e.g., strain softening), and geochemical (e.g., leaching). A compilation of the properties of weak layers observed in submarine landslide studies [*Locat et al*., 2014] shows that there is no common element and that there can be various sediment types and failure processes involving weak layers. However, this study, along with results from other large mass movements on the Norwegian continental margin, clearly documents the significance of muddy contourites with respect to submarine slope stability. The weak layer of the

Trænadjupet Slide contains interstadial hemipelagic and/or contouritic sediments [*Laberg et al*., 2002]. Also in the Nyk slide, one or more glide planes of the slide are located within the contourite drift and are parallel to the original acoustic lamination [*Lindberg et al*., 2004]. In the Storegga slide, the laterally extensive glide planes lie within the hemipelagic/contouric marine clays characterized by strain-softening behavior [*Bryn et al*., 2005].

Contouritic sediments are prone to failure because of their composition (well-sorted muddy or sandy sediments), high-sedimentation rates (high water content), rapid loading, and often excess pore pressure development [*Laberg and Camerlenghi*, 2008]. The properties of contouritic sediments also favor the development of strain-softening behavior and the potential for progressive failure along extensive, nearly flat rupture surfaces. This mechanism was proposed to explain the large spread failures observed near the head of the Storegga Slide [*Kvalstad et al*., 2005].

This study furthermore illustrates the significance of contourites on submarine slope stability also for smaller-scale mass movements in areas not affected by rapid loading of glacigenic sediments resulting in the development of excess pore pressure. Rapid loading of glacigenic sediments is often seen as a prerequisite for large landslides on high-latitude and passive continental margins [*Bryn et al*., 2005; *Laberg and Camerlenghi*, 2008]. Instead, the prefailure slope morphology including older headwalls and/or escarpments indicates a long history of sediment failure, which may have influenced the stability of contouritic sediments, leading to the failure of the uppermost part (~12 m) following an external trigger.

5.3.2. Sedimentation Rates and Excess Pore Pressure

Excess pore pressure generation due to high sedimentation during peak glacial has been suggested to be an important precondition to failure within the large submarine landslides on the Norwegian continental margin [e.g., *Bryn et al*., 2005; *Kvalstad et al*., 2005; *Leynaud et al*., 2009]. Rapid loading of fine-grained sediments may well cause underconsolidation as excess pore pressure developing during sedimentation cannot easily dissipate (depending on the soil's permeability). The undrained shear strength of the sediments during the consolidation process depends on the excess pore pressure dissipation [e.g., *Leynaud et al*., 2009]. In the study area, average sedimentation rates have been relatively low (up to 4 m/ka), compared to sedimentation rates of 65 m/ka for the glacigenic sediments within the Trænadjupet area [*Laberg et al*., 2003]. We therefore do not expect that excess pore pressure was generated nor has played a significant role in the stability of the continental slope sediments.

5.3.3. Gas and Gas Hydrate Dissociation

Often, shallow gas and hydrate dissociation (e.g., caused by climate-controlled variations in pressure and temperature conditions) are considered to play a critical role in preconditioning or triggering slope failures. The presence of gas bubbles affects the compressibility of the soils and may cause pore pressure buildup. Likewise, hydrate dissociation into gas and water would lead to excess pore pressures [e.g., *Mosher et al*., 2004; *Mienert et al*., 2005; *Lee*, 2009; *Leynaud et al*., 2009]. However, neither the geophysical data nor the core samples show indications of gas or hydrates. We are not aware of publications that report either direct or indirect evidence of gas hydrates in the immediate vicinity of the landslides studied here. Furthermore, the interpreted retrogressive landslide development in which multiple slip planes are utilized is at odds with hydrate dissociation as a preconditioning factor. We therefore consider that gas or hydrates are, based on the currently available information, unlikely candidates to affect the stability of the continental slope in the study area.

5.4. Triggering Mechanisms

Many submarine landslides require an external trigger. The landslide simulations presented in this study reveal that the sediment displacements (Figure 3) can be reconstructed for present-day conditions when using the remolded shear strength. This implies that a progressive spreading of strain softening can develop in this area when initiated by an external trigger, which will be further discussed below.

Earthquakes are among the most obvious and best known triggering mechanisms for submarine slides [e.g., *Leynaud et al*., 2009]. At high latitudes, earthquakes can result from tectonic movements and glacioisostatic readjustment during and following the deglaciation of the large ice sheets [e.g., *Gudmundsson*, 1999; *Bryn et al*., 2003; *Bungum et al*., 2005; *Lee*, 2009]. Seismic activity offshore Fennoscandinavia was higher following the isostatic rebound from 10 ka to the present [*Bungum et al*., 2005] and was inferred to be the most likely triggering mechanism for both the Storegga Slide [*Kvalstad et al*., 2005] and the Trænadjupet Slide [*Laberg and Vorren*, 2000].

Small-scale submarine mass movements that have affected the Vesterålen margin (north of our study area) have possibly been triggered by earthquakes following the last glaciation due to isostatic uplift [*L'Heureux et al*., 2013]. Results from pseudostatic analyses, dynamic analysis, and postearthquake pore pressure dissipation show that severe earthquake loading with a very low probability of occurrence or repeated earthquake activity was necessary for these mass movements to occur [*L'Heureux et al*., 2013]. A similar scenario is also favored for the triggering of the mass movements of this study.

One critical observation from the geophysical data is the proximity of a larger landslide complex immediately downslope of the instabilities described in this study (see Figure 2). Therefore, a causal link between the smaller-scale instabilities and the larger mass movement complex is likely and was a key argument to investigate the stability using a retrogressive landslide model. The data suggest that the larger mass movement complex predates the smaller-scale mass movements (Figures 2 and 3) [*Baeten et al*., 2013] and can be seen to undercut the foot of the slope causing a loss of support of the sediments upslope. This, in turn, may trigger retrogressive movement in response to progressive spreading of strain softening along the slide base and in the slide mass (Figure 12d).

6. Conclusions

1. Shallow mass movements on the continental slope off northern Norway consist of three zones: in zone 1, a fracture forms due to initial movement of a mostly undisturbed slab of sediments for a short distance; in zone 2, the fracture widens several tens of meters and develops into a shallow graben structure without major disintegration or deformation of the slab; and in zone 3, most of the slab disintegrates into a number of smaller internally disturbed/deformed slabs and blocks.
2. A 16 m long calypso core containing mostly undisturbed massive and laminated, ice-rafted debris-rich clay penetrated a zone 1 slab.
3. The core penetrated a high-amplitude semicontinuous reflection visible on the subbottom profiler data at about 12.5 m depth, correlated to the interface between a plumite interval and contouritic sediments above, inferred to have acted as the basal glide plane.
4. This plumite consists of silty clay with silty laminae, has dilative behavior with pore pressure decrease with increasing shear strain and high undrained shear strength, and was deposited by meltwater plumes during the LGM.
5. Movement presumably started within contouritic sediments above, consisting of laminated clay deposited during the LGM, when the ice front was situated at the shelf edge.
6. The properties of the contouritic sediments influence the stability of the continental slope also outside areas of rapid loading of glacigenic sediments, a prerequisite for the large submarine landslides on high-latitude and passive continental margins. The combination of the weaker contouritic sediments directly above the stonger plumite is considered to be an important preconditioning factor in the study area.
7. The simulations with the infinite slope model, the BING model, and the retrogressive slope model show that it is possible to reconstruct the mass movements when using present-day conditions, if the mass movement is initiated by an external trigger.
8. Whereas it is often difficult to pinpoint the actual triggering mechanism, we believe that the external trigger for the landslides studied here is either an earthquake, the undercutting at the foot of the slope and a loss of support of the overlying sediments, or a combination of the two. The undercutting at the foot of the slope consequently lead to retrogressive movement upslope and progressive spreading of strain softening along the slide base and in the slide mass.
9. The present-day continental slope is considered stable with a factor of safety of approximately 4.

Acknowledgments

This work is a contribution to the project Seafloor stability offshore Lofoten, northern Norway, (LOSLOPE), funded by the Research Council of Norway, and the UNESCO program Training Through Research. We are grateful to Statoil for financial support and to the captains and crew and participants of scientific cruises on R/V *Professor Logachev*, R/V *Jan Mayen* (now *Helmer Hanssen*), and R/V *G.O. Sars*, especially Steinar Iversen for essential support during the acquisition of data, to Trine Dahl, Edel Ellingsen, and Kristine Hansen for their help in the lab, and to Jan P. Holm for help with the first figure. Special thanks to Kevin McKillop, Calvin Campbell, David Piper, David Mosher, and Francky Saint-Ange at the Bedford Institute of Oceanography, Halifax, Canada, where part of this paper was written during a 5 months visit, Dieter Issler, Jean-Sebastien L'Heureux, and Siren Knudsen at NGI for fruitful discussions and designing the geotechnical laboratory tests; and Michail Ivanov (deceased) for his efforts in organizing the TTR-17 cruise. We also acknowledge NGI's laboratory for the geotechnical tests and CT scans. This is publication 434 for the International Centre of Geohazards, Oslo. This paper is dedicated to the memories of Tore O. Vorren and Michail Ivanov.

References

Andersen, B. G. (1975), Glacial geology of northern Nordland, north Norway, *Nor. Geol. Unders.*, *320*, 1–74.

Auffret, G., S. Zaragosi, B. Dennielou, E. Cortijo, D. Van Rooij, F. Grousset, C. Pujol, F. Eynaud, and M. Siegert (2002), Terrigenous fluxes at the Celtic margin during the last glacial cycle, *Mar. Geol.*, *188*, 79–108, doi:10.1016/S0025-3227(02)00276-1.

Baeten, N. J., J. S. Laberg, M. Forwick, T. O. Vorren, M. Vanneste, C. F. Forsberg, T. Kvalstad, and M. Ivanov (2013), Morphology and origin of smaller-scale mass movements on the continental slope off northern Norway, *Geomorphology*, *187*, 122–134, doi:10.1016/j.geomorph.2013.01.008.

Baumann, K.-H., K. S. Lackschewitz, J. Mangerud, R. F. Spielhagen, T. C. W. Wolf-welling, R. Henrich, and H. Kassens (1995), Reflection of Scandinavian ice sheet fluctuations in Norwegian Sea sediments during the past 150,000 years, *Quat. Res.*, *43*, 185–197, doi:10.1006/qres.1995.1019.

Blindheim, J. (1990), Arctic intermediate water in the Norwegian Sea, *Deep Sea Res., Part A*, *37*, 1475–1489, doi:10.1016/0198-0149(90)90138-L.
Bryn, P., A. Solheim, K. Berg, R. Lien, C. F. Forsberg, H. Haflidason, D. Ottesen, and L. Rise (2003), The Storegga Slide complex: Repeated large scale sliding in response to climatic cyclicity, in *Submarine Mass Movements and Their Consequences*, edited by J. Locat and J. Mienert, pp. 215–222, Kluwer Acad. Press, Netherlands, doi:10.1007/978-94-010-0093-2_24.
Bryn, P., K. Berg, C. F. Forsberg, A. Solheim, and T. Kvalstad (2005), Explaining the Storegga Slide, *Mar. Pet. Geol.*, *22*, 11–19, doi:10.1016/j.marpetgeo.2004.12.003.
Bugge, T. (1983), *Submarine Slides on the Norwegian Continental Margin, With Special Emphasis on the Storegga Area*, *Publ.*, vol. 110, pp. 152, The Continental Shelf and Petroleum Research Institute, Trondheim, Norway.
Bungum, H., C. Lindholm, and J. I. Faleide (2005), Postglacial seismicity offshore mid-Norway with emphasis on spatio-temporal-magnitudal variations, *Mar. Pet. Geol.*, *22*, 137–148, doi:10.1016/j.marpetgeo.2004.10.007.
Canals, M., et al. (2004), Slope failure dynamics and impacts from seafloor and shallow sub-seafloor geophysical data: An overview, *Mar. Geol.*, *213*, 9–72, doi:10.1016/j.margeo.2004.10.001.
Casagrande, A. (1936), The determination of the pre-consolidation load and its practical significance, in *Proceedings of the International Conference on Soil Mechanics and Foundation Engineering*, vol. 3, edited by A. Casagrande, P. C. Rutledge, and J. D. Watson, pp. 60–64, *Am. Soc. Civ. Eng.*, Cambridge, Mass.
Dahlgren, T. K. I., and T. O. Vorren (2003), Sedimentary environment and glacial history during the last 40 ka of the Vøring continental margin, mid-Norway, *Mar. Geol.*, *193*(1–2), 93–127, doi:10.1016/S0025-3227(02)00617-5.
Dan, G., N. Sultan, and B. Savoye (2007), The 1979 Nice harbour catastrophe revisited: Trigger mechanism inferred from geotechnical measurements and numerical modeling, *Mar. Geol.*, *245*, 40–64, doi:10.1016/j.margeo.2007.06.011.
De Blasio, F. V., D. Issler, A. Elverhøi, C. B. Harbitz, T. Ilstad, P. Bryn, R. Lien, and F. Løvholt (2003), Dynamics, velocity and run-out of the giant Storegga slide, in *Submarine Mass Movements and Their Consequences*, edited by J. Locat and J. Mienert, pp. 223–230, Kluwer Acad. Press, Netherlands, doi:10.1007/978-94-010-0093-2_25.
De Blasio, F. V., A. Elverhøi, D. Issler, C. B. Harbitz, P. Bryn, and R. Lien (2005), On the dynamics of subaqueous clay rich gravity mass flows—The giant Storegga slide, Norway, *Mar. Pet. Geol.*, *22*, 179–186, doi:10.1016/j.marpetgeo.2004.10.014.
Embley, R. W. (1980), The role of mass transport in the distribution and character of deep ocean sediments with special reference to the North Atlantic, *Mar. Geol.*, *38*, 23–50, doi:10.1016/0025-3227(80)90050-X.
Föhn, P. M. B., C. Camponovo, and G. Krusi (1998), Mechanical and structural properties of weak snow layers measured in situ, *Ann. Glaciol.*, *26*, 1–6.
Gudmundsson, A. (1999), Postglacial crustal doming, stresses and fracture formation with application to Norway, *Tectonophysics*, *307*, 407–419, doi:10.1016/S0040-1951(99)00107-9.
Haflidason, H., H. P. Serjup, I. M. Berstad, A. Nygard, T. Richter, P. Bryn, R. Lien, and K. Berg (2003), A weak layer feature on the northern Storegga slide escarpment, in *European Margin Sediment Dynamics*, edited by J. Mienert and P. P. E. Weaver, pp. 37–43, Springer, Berlin, doi:10.1007/978-3-642-55846-7_7.
Haflidason, H., H. P. Sejrup, A. Nygård, J. Mienert, P. Bryn, R. Lien, C. F. Forsberg, K. Berg, and D. Masson (2004), The Storegga Slide: Architecture, geometry and slide development, *Mar. Geol.*, *213*, 201–234, doi:10.1016/j.margeo.2004.10.007.
Haflidason, H., M. M. Alvaro, A. Nygard, H. P. Sejrup, and J. S. Laberg (2007), Holocene sedimentary processes in the Andøya Canyon system, north Norway, *Mar. Geol.*, *246*, 86–104, doi:10.1016/j.margeo.2007.06.005.
Hald, M., and R. Aspeli (1997), Rapid climatic shifts of the northern Norwegian Sea during the last deglaciation and the Holocene, *Boreas*, *26*, 15–28, doi:10.1111/j.1502-3885.1997.tb00648.x.
Hampton, M. A., H. J. Lee, and J. Locat (1996), Submarine landslides, *Rev. Geophys.*, *34*(1), 33–59, doi:10.1029/95RG03287.
Hesse, R., S. Khodabakhsh, I. Klaucke, and W. B. F. Ryan (1997), Asymmetrical turbid surface-plume deposition near ice-outlets of the Pleistocene Laurentide ice sheet in the Labrador Sea, *Geo Mar. Lett.*, *17*, 179–187, doi:10.1007/s003670050024.
Hjelstuen, B. O., H. P. Sejrup, H. Haflidason, A. Nygård, L. M. Berstad, and G. Knorr (2004), Late Quaternary seismic stratigraphy and geological development of the south Vøring Margin, Norwegian Sea, *Quat. Sci. Rev.*, *23*, 1847–1865, doi:10.1016/j.quascirev.2004.03.005.
Hungr, O., S. Leroueil, and L. Picarelli (2014), The Varnes classification of landslide types, an update, *Landslides*, *11*(2), 167–194, doi:10.1007/s10346-013-0436-y.
Huvenne, V. A. I., P. F. Croker, and J.-P. Henriet (2002), A refreshing 3D view of an ancient sediment collapse and slope failure, *Terra Nova*, *14*, 33–40, doi:10.1046/j.1365-3121.2002.00386.x.
Imran, J., P. Harff, and G. Parker (2001), A numerical model of submarine debris flow with graphical user interface, *C. R. Geosci.*, *27*, 717–729, doi:10.1016/S0098-3004(00)00124-2.
Issler, D., F. V. De Blasio, A. Elverhøi, and T. Ilstad (2003), Issues in the assessment of gravity mass flow hazard in the Storegga area of the western Norwegian coast, in *Submarine Mass Movements and Their Consequences*, edited by J. Locat and J. Mienert, pp. 231–238, Kluwer Acad. Press, Netherlands, doi:10.1007/978-94-010-0093-2_26.
Issler, D., F. V. De Blasio, A. Elverhøi, P. Bryn, and R. Lien (2005), Scaling behaviour of clay-rich submarine debris flows, *Mar. Pet. Geol.*, *22*, 187–194, doi:10.1016/j.marpetgeo.2004.10.015.
Jakobsson, M., et al. (2012), The International Bathymetric Chart of the Arctic Ocean (IBCAO) version 3.0, *Geophys. Res. Lett.*, *39*, L12609, doi:10.1029/2012GL052219.
Kenyon, N. H. (1987), Mass-wasting features on the continental slope of northwest Europe, *Mar. Geol.*, *74*, 57–77, doi:10.1016/0025-3227(87)90005-3.
Krastel, S., R. B. Wynn, A. Georgiopoulou, J. Geersen, R. Henrich, M. Meyer, and T. Schwenk (2012), Large-scale mass wasting on the northwest African continental margin: Some general implications for mass wasting on passive continental margins, in *Submarine Mass Movements and Their Consequences, Adv. Nat. Technol. Hazard Res.*, vol. 31, edited by Y. Yamada et al., pp. 189–199, Springer, Dordrecht, Netherlands, doi:10.1007/978-94-007-2162-3_17.
Kvalstad, T. J., F. Nadim, A. M. Kaynia, K. H. Mokkelbost, and P. Bryn (2005), Soil conditions and slope stability in the Ormen Lange area, *Mar. Pet. Geol.*, *22*, 245–256, doi:10.1016/j.marpetgeo.2004.10.021.
L'Heureux, J. S., A. Steiner, O. Longva, S. Chand, M. Vanneste, A. Kopf, H. Haflidason, T. Kvalstad, C. F. Forsberg, and M. E. Vardy (2012), Identification of weak layers and their role for the stability of slopes at Finneidfjord, northern Norway, in *Submarine Mass Movements and Their Consequences, Adv. Nat. Technol. Hazard Res.*, vol. 31, edited by Y. Yamada et al., pp. 321–330, Springer, Dordrecht, Netherlands, doi:10.1007/978-94-007-2162-3_29.
L'Heureux, J. S., M. Vanneste, L. Rise, J. Brendryen, C. F. Forsberg, F. Nadim, O. Longva, S. Chand, T. J. Kvalstad, and H. Haflidason (2013), Stability, mobility and failure mechanism for landslides at the upper continental slope off Vesterålen, Norway, *Mar. Geol.*, *346*, 192–207, doi:10.1016/j.margeo.2013.09.009.

Laberg, J. S., and A. Camerlenghi (2008), The significance of contourites for submarine slope stability, in *Countourites, Developments in Sedimentology*, vol. 60, edited by M. Rebesco and A. Camerlenghi, pp. 537–556, Elsevier, Netherlands, doi:10.1016/S0070-4571(08)10025-5.

Laberg, J. S., and T. O. Vorren (2000), The Trænadjupet Slide, offshore Norway—Morphology, evacuation and triggering mechanisms, *Mar. Geol.*, *171*, 95–114, doi:10.1016/S0025-3227(00)00112-2.

Laberg, J. S., and T. O. Vorren (2004), Weichselian and Holocene growth of the northern high-latitude Lofoten Contourite Drift on the continental slope of Norway, *Sediment. Geol.*, *164*, 1–17, doi:10.1016/j.sedgeo.2003.07.004.

Laberg, J. S., T. O. Vorren, and S.-M. Knutsen (1999), The Lofoten Contourite drift off Norway, *Mar. Geol.*, *159*, 1–6, doi:10.1016/S0025-3227(98)00198-4.

Laberg, J. S., T. Dahlgren, T. O. Vorren, H. Haflidason, and P. Bryn (2001), Seismic analyses of Cenozoic contourite drift development in the northern Norwegian Sea, *Mar. Geophys. Res.*, *22*, 401–416, doi:10.1023/A:1016347632294.

Laberg, J. S., T. O. Vorren, J. Mienert, P. Bryn, and R. Lien (2002), The Trænadjupet Slide: A large slope failure affecting the continental margin of Norway 4000 years ago, *Geo Mar. Lett.*, *22*, 19–24, doi:10.1007/s00367-002-0092-z.

Laberg, J. S., T. O. Vorren, J. Mienert, H. Haflidason, P. Bryn, and R. Lien (2003), Preconditions leading to the Holocene Trænadjupet Slide offshore Norway, in *Submarine Mass Movements and Their Consequences*, edited by J. Locat and J. Mienert, pp. 215–222, Kluwer Acad. Press, Netherlands, doi:10.1007/978-94-010-0093-2_28.

Laberg, J. S., T. O. Vorren, N. H. Kenyon, and M. Ivanov (2006), Frequency and triggering mechanisms of submarine landslides of the north Norwegian continental margin, *Norw. J. Geol.*, *86*, 155–161.

Laberg, J. S., R. S. Eilertsen, G. R. Salomonsen, and T. O. Vorren (2007), Submarine push moraine formation during the early Fennoscandian Ice Sheet deglaciation, *Quat. Res.*, *67*, 453–462, doi:10.1016/j.yqres.2007.01.014.

Lastras, G., M. Canals, R. Urgeles, J. E. Hughes-Clarke, and J. Acosta (2004), Shallow slides and pockmarks swarms in the Eivissa Channel, western Mediterranean Sea, *Sedimentology*, *51*, 1–14, doi:10.1111/j.1365-3091.2004.00654.x.

Lauritzen, S.-E. (1991), Uranium series dating of speleothems: A glacial chronology for Nordland, Norway for the last 600 ka, *Striae*, *34*, 127–133.

Lee, H. J. (2009), Timing of occurrence of large submarine landslides on the Atlantic Ocean margin, *Mar. Geol.*, *264*, 53–64, doi:10.1016/j.margeo.2008.09.009.

Lehman, S. J., G. A. Jones, L. D. Keigwin, E. S. Anderson, G. Butenko, and S.-R. Østmo (1991), Initiation of Fennoscandian Ice-Sheet retreat during the last deglaciation, *Nature*, *349*, 513–516, doi:10.1038/349513a0.

Lekens, W., H. P. Sejrup, H. Haflidason, G. Ø. Petersen, B. O. Hjelstuen, and G. Knorr (2005), Laminated sediments preceding Heinrich event 1 in the Northern North Sea and Southern Norwegian Sea, origin, processes and regional linkage, *Mar. Geol.*, *216*, 27–50, doi:10.1016/j.margeo.2004.12.007.

Leynaud, D., J. Mienert, and M. Vanneste (2009), Submarine mass movements on glaciated and non-glaciated European continental margins: A review of triggering mechanisms and preconditions to failure, *Mar. Pet. Geol.*, *26*, 618–632, doi:10.1016/j.marpetgeo.2008.02.008.

Lindberg, B., J. S. Laberg, and T. O. Vorren (2004), The Nyk Slide—Morphology, progression, and age of a partly buried submarine slide offshore mid-Norway, *Mar. Geol.*, *213*, 277–289, doi:10.1016/j.margeo.2004.10.010.

Locat, J., H. J. Lee, P. Locat, and J. Imran (2004), Numerical analysis of the mobility of the Palos Verdes debris avalanche, California, and its implications for the generation of tsunamis, *Mar. Geol.*, *203*, 269–280, doi:10.1016/S0025-3227(03)00310-4.

Locat, J., S. Leroueil, A. Locat, and H. Lee (2014), Weak layers: Their definition and classification from a geotechnical perspective, in *Submarine Mass Movements and Their Consequences*, *Adv. Nat. Technol. Hazard Res.*, vol. 37, edited by S. Krastel et al., pp. 3–12, Springer, Dordrecht, Netherlands, doi:10.1007/978-3-319-00972-8_1.

Lucchi, R. G., M. T. Predrosa, A. Camerlenghi, R. Urgeles, B. De Mol, and M. Rebesco (2012), Recent submarine landslides on the continental slope of Storfjorden and Kveithola trough-mouth fans (North West Barents Sea), in *Submarine Mass Movements and Their Consequences*, *Adv. Nat. Technol. Hazards Res.*, vol. 31, edited by Y. Yamada et al., pp. 735–745, Springer, Dordrecht, Netherlands, doi:10.1007/978-94-007-2162-3_65.

Lucchi, R. G., et al. (2013), Postglacial sedimentary processes on the Storfjorden and Kveithola trough mouth fans: Significance of extreme glacimarine sedimentation, *Global Planet. Change*, *111*, 309–326, doi:10.1016/j.gloplacha.2013.10.008.

Lunne, T., P. K. Robertson, and J. J. M. Powell (1997), *Cone Penetration Testing in Geotechnical Practice*, pp. 45–148, Spon Press, London and New York.

Lykousis, V., G. Roussakis, and D. Sakellariou (2009), Slope failures and stability analysis of shallow water prodeltas in the active margins of Western Greece, northeastern Mediterranean Sea, *Int. J. Earth Sci. (Geol Rundsch)*, *98*, 807–822, doi:10.1007/s00531-008-0329-9.

Masson, D. G., R. B. Wynn, and P. J. Talling (2010), Large landslides on passive continental margins: Processes, hypotheses and outstanding questions, in *Submarine Mass Movements and Their Consequences*, *Adv. Nat. Technol. Hazards Res.*, vol. 28, edited by D. C. Mosher et al., pp. 153–165, Springer, Dordrecht, Netherlands, doi:10.1007/978-90-481-3071-9_13.

Mienert, J., S. Bünz, S. Guidard, M. Vanneste, and C. Berndt (2005), Ocean bottom seismometer investigations in the Ormen Lange area offshore mid-Norway provide evidence for shallow gas layers in subsurface sediments, *Mar. Pet. Geol.*, *22*, 287–297, doi:10.1016/j.marpetgeo.2004.10.020.

Mix, A., E. Bard, and R. Schneider (2001), Environmental processes of the Ice age: Land, ocean glaciers (EPILOG), *Quat. Sci. Rev.*, *20*, 627–658, doi:10.1016/S0277-3791(00)00145-1.

Mosher, D. C., D. J. W. Piper, D. C. Campbell, and K. A. Jenner (2004), Near-surface geology and sediment-failure geohazards of the central Scotian Slope, *AAPG Bull.*, *88*(6), 703–723, doi:10.1306/01260403084.

O'Leary, D. W. (1996), The timing and spatial relations of submarine canyon erosion and mass movement on the New England continental slope and rise, in *Geology of the United States' Seafloor: The View From GLORIA*, edited by J. V. Gardner et al., pp. 47–58, Cambridge Univ. Press, Cambridge, U. K.

Olsen, L., H. Sveian, and B. Bergstrøm (2001), Rapid adjustment of the western part of the Scandinavian Ice Sheet during the mid- and late Weichselian—A new age model, *Norw. J. Geol.*, *81*, 93–118.

Piper, D. J. W., P. Cochonat, and M. L. Morrison (1999), The sequence of events around the epicenter of the 1929 Grand Banks earthquake: Initiation of debris flows and turbidity currents inferred from sidescan sonar, *Sedimentology*, *46*, 79–97, doi:10.1046/j.1365-3091.1999.00204.x.

Poulain, P.-M., A. Warn-Varnas, and P. P. Niiler (1996), Near-surface circulation of the Nordic Seas as measured by Lagrangian drifters, *J. Geophys. Res.*, *101*(C8), 18,237–18,258, doi:10.1029/96JC00506.

Rebesco, M., M. T. Predrosa, A. Camerlenghi, R. G. Lucchi, C. Sauli, B. De Mol, G. Madrussani, R. Urgeles, G. Rossi, and G. Böhm (2012), One million years of climatic generated landslide events on the northwestern Barents Sea continental margin, in *Submarine Mass Movements and Their Consequences*, *Adv. Nat. Technol. Hazards Res.*, vol. 31, edited by Y. Yamada et al., pp. 747–756, Springer, Dordrecht, Netherlands, doi:10.1007/978-94-007-2162-3_66.

Reimer, P. J., et al. (2009), IntCal and Marine09 radiocarbon age calibration curves, 0-50,000 years cal BP, *Radiocarbon*, *51*, 1111–1150, doi:10.2458/azu_js_rc.55.16947.

Rise, L., S. Chand, H. Haflidason, J.S. L'Heureux, B.O. Hjelstuen, V. Bellec, O. Longva, J. Brendryen, M. Vanneste, and R. Bøe (2012), Investigations of slides at the upper continental slope off Vesterålen, North Norway, in *Submarine Mass Movements and Their Consequences*, *Adv. Nat. Technol. Hazards Res.*, vol. 31, edited by Y. Yamada et al., pp. 167–176, Springer, Dordrecht, Netherlands, doi:10.1007/978-94-007-2162-3_15.

Rørvik, K.-L., J. S. Laberg, M. Hald, E. K. Ravna, and T. O. Vorren (2010), Behavior of the northwestern part of the Fennoscandian Ice Sheet during the Last Glacial Maximum—A response to external forcing, *Quat. Sci. Rev.*, *29*, 2224–2237, doi:10.1016/j.quascirev.2010.05.022.

Solheim, A., K. Berg, C. F. Forsberg, and P. Bryn (2005), The Storegga Slide complex: Repetitive large scale sliding with similar cause and development, *Mar. Pet. Geol.*, *22*, 97–107, doi:10.1016/j.marpetgeo.2004.10.013.

Stuiver, M., and P. J. Reimer (1993), Extended 14C database and revised CALIB radiocarbon calibration program, *Radiocarbon*, *35*, 215–230.

Swift, J. H., and K. P. Koltermann (1988), The origin of Norwegian Sea deep water, *J. Geophys. Res.*, *93*(C4), 3563–3569, doi:10.1029/JC093iC04p03563.

Széréméta, N., F. Bassinot, Y. Balut, L. Labeyrie, and M. Pagel (2004), Oversampling of sedimentary series collected by giant piston corer: Evidence and corrections based on 3.5-kHz chirp profiles, *Paleoceanography*, *19*, PA1005, doi:10.1029/2002PA000795.

Thomsen, E., and T. O. Vorren (1986), Macrofaunal paleoecology and stratigraphy in late Quaternary shelf sediments off northern Norway, *Paleogeogr. Paleoclimateol. Paleoecol.*, *56*, 103–150, doi:10.1016/0031-0182(86)90110-0.

Trincardi, F., A. Cattaneo, and A. Correggiari (2004), Mediterranean prodelta systems: Natural evolution and human impact investigated by EURODELTA, *Oceanography*, *17*, 34–45.

Tripsanas, E. K., and D. J. W. Piper (2008), Glaciogenic debris-flow deposits of orphan basin, offshore Eastern Canada: Sedimentological and rheological properties, origin, and relationship to meltwater discharge, *J. Sediment. Res.*, *78*, 724–744, doi:10.2110/jsr.2008.082.

Vanneste, M., J. Mienert, and S. Bünz (2006), The Hinlopen Slide: A giant, submarine slope failure on the northern Svalbard margin, Arctic Ocean, *Earth Planet. Sci. Lett.*, *245*, 373–388, doi:10.1016/j.epsl.2006.02.045.

Vanneste, M., et al. (2013), Finneidfjord: A field laboratory for integrated submarine slope stability assessments and characterization of landslide-prone sediments: A Review, in OTC 2013: Proceedings of 44th Offshore Technology Conference. Offshore Technology Conference, 23967-MS, Richardson, US, Offshore Technology Conference, doi:10.4043/23967-MS.

Vorren, T. O., M. Hald, and E. Thomsen (1984), Quaternary sediments and environments on the continental shelf off northern Norway, *Mar. Geol.*, *57*, 229–257, doi:10.1016/0025-3227(84)90201-9.

Vorren, T. O., J. S. Laberg, F. Blaume, J. A. Dowdeswell, N. H. Kenyon, J. Mienert, J. Rumohr, and F. Werner (1998), The Norwegian-Greenland Sea continental margins: Morphology and Late Quaternary sedimentary processes and environment, *Quat. Sci. Rev.*, *17*, 273–302, doi:10.1016/S0277-3791(97)00072-3.

Vorren, T. O., K.-D. Vorren, O. Aasheim, K. I. T. Dahlgren, M. Forwick, and K. Hassel (2013), Palaeoenvironment in northern Norway between 22.2 and 14.5 cal. ka, *Boreas*, *42*, 876–895, doi:10.1111/bor.12013.

Wessel, P., and W. H. F. Smith (1998), New, improved version of Generic Mapping Tools released, *EOS Trans. AGU*, *79*, 579, doi:10.1029/98EO00426.

Yoon, S. H., S. K. Chough, J. Thiede, and F. Werner (1991), Late Pleistocene sedimentation on the Norwegian continental slope between 67° and 71° N, *Mar. Geol.*, *99*, 187–207, doi:10.1016/0025-3227(91)90091-H.